

Numerical Modelling of the Effects of High Strain Rate, Strain Path and Particles on the Formability of FCC Polycrystals

by

Jonathan Rossiter

A thesis
presented to the University of Waterloo
in fulfillment of the
thesis requirement for the degree of
Master of Applied Science
in
Mechanical Engineering
Waterloo, Ontario, Canada, 2009

© Jonathan Rossiter 2009

Author's Declaration

I hereby declare that I am the sole author of this thesis. This is a true copy of the thesis, including any required final revisions, as accepted by my examiners.

I understand that my thesis may be made electronically available to the public.

Abstract

A new crystal plasticity scheme for explicit time integration codes is developed based on a forward Euler algorithm in the first part of this paper. The new numerical model is incorporated in the UMAT subroutine for implementing rate dependent crystal plasticity model in LS-DYNA/Explicit. The material is modeled as a Face centered cubic (FCC) polycrystalline aggregate, and a finite element analysis based on rate-dependent crystal plasticity is developed to simulate large strain behaviour. Accordingly, an element or a number of elements of the finite element mesh is considered to represent a single crystal within the polycrystal aggregate and the constitutive response at a material point is given by the single crystal constitutive model. The second part of this thesis presents two applications of the crystal plasticity scheme used in conjunction with numerical modeling of three-dimensional (3D) real microstructures. First, finite element meshes containing both particle and texture data are created with solid elements. Particle size, location and orientation are represented by 3D ellipsoids and the elements within these ellipsoids are given rigid properties. Simulations of in-plane plane strain with different combinations of texture and particle location are performed. The effect on texture development, strain magnitudes, and strain localizations is investigated. Second, the three dimensional (3D) polycrystalline microstructure of the aluminum alloy AA5754 is modeled and subjected to three different strain rates for each strain path. The effect of strain paths, strain rates and thermal softening on the formation of localized deformation is investigated. Simulations show that strain path is the most dominant factor in localized deformation and texture evolution.

Acknowledgements

This work was supported by the Natural Sciences and Engineering Research Council of Canada (NSERC) and General Motors of Canada. I also gratefully acknowledge the high performance computing center at the University of Sherbrooke, and Dr HuiZhong Lu from the Reseau Quebecois de Calcul de Haute Performance (RQCHP) for his technical support. I would also like to acknowledge the help of Dr. Asim Tewari to incorporate the 3D particle data into the numerical model, Dr. Abhijit Brahme for providing the microstructure data, and Mr. Simha for executing the cpu timing experiments. Finally I would like to thank my supervisor Prof. Kaan Inal for his constant help throughout the entire process.

Table of Contents

List of Figures.....	vii
List of Tables	ix
1. Introduction	1
2. Crystal Plasticity Theory	7
2.1 Single crystal deformation models.....	8
2.1.1 Rate-insensitive deformation	8
2.2 Deformation textures.....	8
2.3 General introduction of polycrystal deformation models.	9
2.3.1 Sachs' model.....	10
2.3.2 The Taylor criterion	11
2.3.3 The Taylor assumptions.....	12
2.3.4 Relaxed constraint models	13
2.3.5 Self-consistent schemes	14
2.4 Discussion and Conclusion	14
2.5 New Developments in Crystal Plasticity Theory and Their Applications	16
2.5.1 Models including interactions between grains.....	16
2.5.2 Strain gradient plasticity	18
2.5.3 Models including backstress.....	20
2.5.4 Discrete dislocation plasticity.....	21
3. Constitutive Model	23
3.1 Orientation Update	27
4. Numerical Implementation.....	28
4.1 Time Integration methods	28
4.1.1 Rate tangent modulus method.....	28
4.1.2 Forward Euler Algorithm.....	29
4.1.3 Validation of the Forward Euler Algorithm.....	31

4.1.4	Comparisons of CPU Times: The Rate Tangent versus the Forward Euler Methods	34
4.2	Construction of Finite Element Model	35
4.2.1	Construction of Microstructure	36
4.2.2	Construction of Mesh	39
5.	Applications	41
5.1	Two-Phase Microstructures	41
5.1.1	Results and Discussions	42
5.2	Shear loading of Al5754	46
5.2.1	Results and Discussion	47
6.	Conclusions	62
	References	65

List of Figures

Figure 1: Decomposition of the deformation gradient F	23
Figure 2: Stress strain curves for uniaxial loading in [001], and [-111] directions.	31
Figure 3: Stress strain curves for uniaxial loading in [-123] direction for $q=1$, and $q=1.4$	32
Figure 4: (a) Accumulated plastic slip on active slip systems, (b) Rotation of slip planes showing latent hardening overshoot for $q = 1.4$	33
Figure 5: Stress Strain of Single Element Simple Shear.....	34
Figure 6: Run Time vs Number of Elements	35
Figure 7: Showing the microstructure generated for the first application using the procedure described in section 4.2.1	37
Figure 8: Pole figure showing the fitted texture for the first application using the procedure outlined in section 4.2.1	37
Figure 9: Showing the microstructure generated for the second application using the procedure described in section 4.2.1 (top layer).	38
Figure 10: Showing the microstructure generated for the second application using the procedure described in section 4.2.1 (center layer).	38
Figure 11: Initial pole figure (a) employed in the procedure outlined in section 4.2.1 and created (b) microstructure used in the second application.....	38
Figure 12: Particle Locations for Second Simulation	41
Figure 13: Particle Locations for Third Simulation	42
Figure 14: Mesh for Second Simulation	42
Figure 15: Maximum Principle Strain with No Particles (First Simulation).	43
Figure 16: Maximum Principle Strain with Particles (Second Simulation).	44
Figure 17: Maximum Principle Strain with Moved Particle (Third Simulation).	44
Figure 18: Max. Prin. Strain For (a) No Particles, (b) Particles, and (c) Moved Particle (4 μ m in).	45
Figure 19: Max. Prin. Strain For (a) No Particles, (b) Particles, and (c) Moved Particle (3 μ m in).	45
Figure 20: Contour Plot of xy strain at 300/s with No Thermal Softening for Simple Shear.	48
Figure 21: Contour Plot of xy strain at 300/s with No Thermal Softening for Tension Followed by Shear.	48
Figure 22: Contour Plot of xy strain at 300/s with No Thermal Softening for Simultaneous Tension and Shear.....	48
Figure 23: Simple Shear Average Stress Strain Curves.....	49
Figure 24: Simultaneous Tension and Shear Average Stress Strain Curves.	50
Figure 25: Tension Followed by Shear Average Stress Strain Curves.....	50
Figure 26: Strain Rise with Thermal Softening vs. Strain without Thermal Softening for Tension Followed by Shear at 3000/s.	52

Figure 27: Contour Plot of the Difference in Effective Strain when Thermal Softening is Added to Tension Followed by Shear at 3000/s.	52
Figure 28: Contour Plot of Effective Strain for Tension Followed by Shear at 3000/s with No Thermal Softening.	53
Figure 29: Contour Plot of Effective Strain for Tension Followed by Shear at 3000/s with Thermal Softening.	53
Figure 30: Contour Plot of Misorientation Change for Simultaneous Tension and Shear at 300/s Without Thermal Softening (center layer).	54
Figure 31: Contour Plot of Misorientation Change for Simultaneous Tension and Shear at 300/s Without Thermal Softening (top layer).	55
Figure 32: Contour Plot of xy Strain for Simultaneous Tension and Shear at 300/s Without Thermal Softening (center layer).	55
Figure 33: Contour Plot of xy Strain for Simultaneous Tension and Shear at 300/s Without Thermal Softening (top layer).	55
Figure 34: Contour Plot of Effective Strain at 12% Simple Shear at 300/s without Thermal Softening.	56
Figure 35: Contour Plot of Effective Strain at 12% Simple Shear at 300/s without Thermal Softening.	56
Figure 36: Contour Plot of Effective Strain at 12% Simple Shear at 300/s without Thermal Softening.	56
Figure 37: Pole Figures of Final Texture for Simple Shear with Thermal Softening for (left to right) a) 300/s, b) 1000/s, c) 3000/s.	57
Figure 38: Pole Figures of Final Texture for Simultaneous Tension and Shear with Thermal Softening for (left to right) a) 300/s, b) 1000/s, c) 3000/s.	57
Figure 39: Pole Figures of Final Texture for Tension Followed by Shear with Thermal Softening for (left to right) a) 300/s, b) 1000/s, c) 3000/s.	58
Figure 40: Showing the local lattice rotation for (a) simultaneous tension and shear and, (b) for tension followed by shear. Comparison shows cube orientation (ND rotated) is more stable than Goss.	59
Figure 41: Showing the comparison between the xystrain for the two different strain paths. (a) Simultaneous tension and shear and (b) tension followed by shear.	59
Figure 42: Showing the exact orientations of some of the near Cube grains.	60
Figure 43: Orientation of grain in region 2 (a) before and (b) after deformation.	60

List of Tables

Table 1: Material Parameters Used in the Simulations.....	31
Table 2: Run Times for Both Rate Tangent and Forward Euler Schemes.....	34
Table 3: Unit Convention.....	42
Table 4: Material Properties.....	46
Table 5: Standard Deviation (SD) of xy strain	51
Table 6: Slope of Strain Rise vs Strain with Thermal Softening.....	53

1. Introduction

It is well known that the localization of plastic flow is strongly influenced by deformation-induced textures and anisotropy (e.g., Hutchinson and Neale [1978a,1978b], Asaro and Needleman [1985]). In turn, this localization is influenced by the real microstructure, especially any heterogeneities as well as actual orientations of grains in three dimensions in a polycrystal. Polycrystal plasticity models with real microstructural input are required to properly simulate plastic instability and localization phenomena. It is expected that such simulations can be more successful in predicting strain localization than can macroscopic phenomenological models, provide an improved understanding of the relation of localization to the microstructure of the material, and can consequently provide guidelines for alloy design to create desirable microstructure for specific applications.

Research in micromechanics has focused on developing single crystal constitutive relationships, such as Asaro and Needleman [1985], Borg [2007], Li et al. [2008], and Zhang et al. [2009], as well as developing computationally efficient correlations based on yield surfaces such as Zamiri et al. [2007]. Numerous numerical simulations were performed where the principle deformation mechanism was considered as crystallographic slip for both FCC and body centered cubic [BCC] structures (e.g., Colvin et al. [2009], and Kuchnicki et al. [2008]). Recent work on hexagonal close packed (HCP) structures has been carried out by researchers such as Lévesque et al. [2009], Beausir et al. [2007], Bridier et al. [2009], Gan and Kysar [2007], Graff et al. [2007], Mayeur and McDowell [2007], and Zhang et al. [2007] where deformation twinning was also introduced as a principle deformation mechanism.

In order to overcome computational limitations, various crystal plasticity models have been implemented into 2D codes and used to simulate plane strain or plane stress deformation states. These models are not capable of predicting strain patterns that are out of plane with the 2D model. Furthermore, it has been shown by Simha et al. [2008] that the state of stress during localized deformation (necking/shear banding) is triaxial, which cannot be modeled using a 2D approach. Due to the advances in parallel computing, the limitations facing the complexity of a simulation are expanding. For this reason, 3D modeling has started becoming more prevalent in works such as Delannay et al. [2006,2008]. The three-dimensional implementation of rate-dependent crystal plasticity models in finite element codes can use explicit time integration as well as implicit time integration. The constitutive update for the rate-dependent crystal plasticity models can be carried out using explicit or implicit schemes. Codes that use implicit time integration afford large time steps and these are usually preferred. Constitutive update in such solvers is through a class implicit integration scheme. Maniatty et al. [1992], Cuitino and Ortiz [1993], Kalidindi et al. [1992], and Raphanel et al. [2004] are examples of implicit constitutive updates implemented in

codes that use implicit time integration. The implementations in an implicit code follow the rate tangent scheme first developed by Peirce et al. [1983]. This scheme requires the inversion of a square matrix whose size is the number of slip systems in the crystallite (the rate tangent scheme belongs to the class of forward gradient schemes, Peirce et al., [1984]). Though such implementations allow for large time steps (and therefore short computational times) they also require the derivation of the material tangent stiffness matrix (material Jacobian). Raphanel et al. [2004] have discussed this approach in detail and derived a second order Runge-Kutta scheme for the constitutive update. As discussed by Raphanel et al. [2004], the derivation of the material Jacobean matrix, which affects the rate of convergence of the global equilibrium equations, is cumbersome.

An alternative approach that does not require the determination of the material Jacobean is the explicit time integration of the momentum equation. In such finite element codes, the unconditionally stable time step is governed by the Courant-Freidrichs-Lewy criterion (Belytschko et al. [2000]), which is governed by the element size and the speed of sound in the material. Consequently, to achieve large deformations in the material, long computational times are required. With the availability of large scale parallel computing, this is not a constraint. Zikry [1994] has implemented rate-dependent crystal plasticity in an FEM code using explicit time integration. His constitutive update uses the Runge-Kutta scheme. More complex schemes such as the homotopy continuation method have been used by Li et al. [2008]. The simplest constitutive implementation in an explicit finite element code appears to be from Kuchnicki et al. [2006]. Here, they use the rate-dependent power law suggested by Cuitino and Ortiz [1993] and an overstress approach that is simple to implement but does require some iteration until the overstress criterion is satisfied on all slip systems. A review of several implicit and explicit constitutive update schemes for rate-dependent crystal plasticity can be found in Ling et al. [2005].

The main focus of this paper is on the numerical implementations of the crystal plasticity based constitutive model proposed by Asaro and Needleman [1985] (which will be summarized briefly later) to finite element method (FEM) applications using a new update scheme and on the application of this new model to simulate the effects of particles in an 3D fcc polycrystalline aggregate. We present a new constitutive update scheme for rate-dependent crystal plasticity laws for use in an explicit finite element code; in particular, the LS-DYNA explicit finite element program (Hallquist, [1998]). It is based on a forward Euler integration scheme of the crystal plasticity framework due to Peirce et al. [1983] and is implemented in an explicit finite element code. We show that the results obtained using this new formulation are comparable to a second-order Runge-Kutta scheme implemented in an implicit finite element code; namely, the implementation due to Raphanel et al. [2004]. Our scheme circumvents the inversion of a matrix (rate tangent scheme), iterations (overstress and other schemes) or the derivation of complex formulas (Runge-Kutta schemes). Results of

simulations using the new scheme are validated by comparing them with published results in the literature. We apply the new model to simulate the effects of particles in a 3D fcc polycrystalline aggregate.

There are multiple ways of modelling a 3D polycrystalline aggregate. Delannay et al. [2006] did a comparison between using 3D bricks with one or more elements per grain, and using 3D truncated octahedrons to represent grains. The comparison was carried out by predicting the texture evolution of a single phase ULC steel, then matching the simulation results with experimental results. The poorest prediction was achieved by using single brick elements to represent each grain. A second brick mesh was used where a 3x3x3 block of cube elements represented each grain. This mesh along with a mesh comprised of truncated octahedrons produced similar, and the best texture predictions. Each truncated octahedron comprised of 16 hexahedral elements distorted in such a way to form a volume filling structure. The simplicity of the 3x3x3 block of cube elements over the truncated octahedron proved to be very attractive. Both the 3x3x3 grid of bricks and the truncated octahedrons represent each grain as exactly the same size, shape, and orientation. An option not compared in the study is to use multiple 3D elements to represent a grain and to contour the boundary of the volume filled by the elements to match the size and shape of the grain. This allows slight variations in grain size, shape and orientation to be represented. Since each octahedron consists of 16 elements, it is only possible to create grains with multiples of 16 elements. Therefore the mesh would need to be incredibly fine in order to model slight differences in grain shape or size. With brick elements, it is possible to create a grain mesh with any whole number of elements. For the applications done in this work, brick elements were used with the number and configuration of those elements tailored specifically for each grain.

The automotive industry is continuously seeking out ways of increasing the desirability of the vehicles they produce. Reducing weight is a very effective method of decreasing the energy required to accelerate and therefore increasing the “stop-and-go” fuel efficiency demanded by modern vocational commuters. Aluminum is an attractive material with a high strength-to-weight ratio and is readily available. With aluminum as the material of construction for the body of the vehicle, significant weight savings can be yielded. As technology advances and forming presses increase in size, huge demand exists for highly formable metals to allow larger and more complicated parts to be produced. By developing an in depth understanding of the materials, optimum alloys and processing can be identified to best suit the part being formed.

Rolled aluminum sheets used in automotive applications are multiphase materials which contain second-phase particles distributed in an aluminum alloy matrix. The distribution, size and shape of these particles depend on the processes that the material has been subjected to. The matrix itself is a collection of grains with specific orientations and

overall texture that are also dependant on the material processing. Numerous studies, both computational and experimental, have examined the effect of particles on formability as well as the effect of voids on the material (e.g. Gan et al. [2006]). Shan et al. [2002] did a study on developing a representative volume element (RVE) for a ceramic matrix composite. They created a statistically equivalent numerical model of a material containing fibres of different sizes as well as fibre-rich and fibre-poor regions. They compared the results of different size RVE's with experimental results and demonstrated that the effect of a heterogeneous material can be modelled using an RVE. Shen et al. [2002] did a comparison between modelling techniques for predicting stress-strain results for materials with particles. The three techniques studied included: single particle 3D unit cell, 3D volume with 45 randomly distributed particles, and 2D models obtained by taking cut sections of the 3D multiple particle model. Aluminum material properties were used for the matrix with ceramic properties used for the particles. The over all stress-strain curves were compared as well as the strain distribution with the simulations. They found that the 2D models predicted very different strain distributions than the 3D multiple particle model did on the same planes. This suggests that when particles are involved, plain strain assumptions are not valid. The over all stress-strain curves were only similar if the area fraction of particles in the 2D model matched the volume fraction of particles in the 3D model. The conclusions drawn were that unit cells and 2D models, while being computationally efficient, were not capable of prediction stress/strain distributions in all cases, and that 3D models were required. Borg et al. [2008] did a study investigated the stress carrying capability of a single crystal with voids. A unit cell approach was taken and the voids were modelled at the sub-micron level. A very thorough investigation was done adjusting void sizes as well as the orientation of the single crystal. The argument was that traditional crystal plasticity models that do not consider length scales were not capable of accurately modelling voids. What was not considered was how the voids reacted with a polycrystalline matrix as opposed to a single crystal. Delannay et al. [2007] investigated transformation induced plasticity (TRIP) steels where they modelled austenite and martensite inclusions in a ferritic matrix. Stress distributions as well as inclusion deformations were calculated using a mean field approach. The hardness of the matrix was varied and the accuracy of each model was tested against experimental data. The models did not take into account the orientation of the matrix in which the inclusions lay. They found a set of simulations that could be modelled accurately and obtained valuable knowledge regarding the TRIP steels and their internal mechanisms. These are important stepping-stones leading to a more complete understanding of the material, although they are only part of the picture. It is important to develop an understanding of how particles interact with the grain texture of the matrix in which they reside. By identifying the processing and alloying that creates the ideal microstructure for inhibiting localization during a given strain situation, the formability of the metal can be greatly improved. In this paper we employ the described numerical model to simulate the effects of particles on heterogeneous deformation in a 3D fcc polycrystalline matrix. Various methods have been used to model particles within

a matrix. Radhakrishnan et al. [2000] used coupled models to allow very small element size surrounding a particle, with larger elements making up the matrix. The complexity of a coupled model is significant. Qu et al. [2005] used cohesive models where the matrix is meshed separately from the particle, and a cohesive layer is used to model the interaction between the particle and single crystal in a unit cell. A 2D approach used by Inal et al. [2008] was to randomly select elements within an element grid and increase the yield strength by a factor of 10, thereby simulating random inclusions equal to the element size. The approach used in this paper is essentially a 3D version of the latter with the exception that a rigid material model is used for the particle elements, the selection of particle elements is controlled and each particle consists of multiple elements. The reason for using this method is that it can be built automatically from serial sectioning data, has the same element resolution at the particles as at the grain interfaces, and can avoid issues caused by highly distorted elements.

In this paper, instead of using serial sectioning data for generating the grain structure, the 3D microstructure is reconstructed from 2D EBSD data following the methods described in Brahme et al. [2007]. The basic hindrance in using the serial sectioning process is the high cost involved and expertise required to obtain the data. Also, from Zaefferer et al. [2008], the techniques are time consuming and the sample volume is limited. The 3D serial sectioning requires either using FIB as in Zaefferer et al. [2008] or metallographical techniques as in Spowart et al. [2003] to expose underlying layers.

The main advantage of the approach used here to obtain 3D microstructure is the relative simplicity as well as time required to generate a new structure. Using the technique we can generate a 3D microstructure with any given shape and size distribution given that we can obtain the above distributions. These distributions can be from a real experimental observation or can be built estimated or expected pseudo microstructure.

To reduce the number of parts required to build a vehicle, the material needs to be capable of straining to large strains in order to contour an increased number of features per part. This high strain capability is where aluminum needs to be improved. Aspects of the forming process such as strain-rate, strain-path, and temperature can be modified and controlled. By gaining an understanding of how these variables can be used to maximize the formability of a material, costs can be minimized.

The limit of formability would be when the material fails. Whether the definition of failure is considered to be localization or material fracture, shear is the dominant failure mode (Lemons and Needleman [1986]). Experimental tests have been done by Gasperini et al. [2001] using a scanning electron microscope (SEM) observed the development of localization during shear. They found that in the rolling direction, very large shear strains

could be obtained. They found that shear bands propagated parallel to the applied load and that typical hardening behaviour took place to promote uniform deformation up to large strains. Physical tests have been created (such as Rauch [1997]) and used by Inal et al. [2002b] to validate 2D simulations which investigate the shear response when loading is at different angles with the rolling direction in sheets. Rauch [1997] developed a shear test that could be implemented in to a tensile testing machine which could use samples cut from a sheet of metal at any angle from rolling direction. A series of stress-strain curves could be developed which could characterize the anisotropy of a given sheet. Crystal plasticity codes developed by Inal et al. could then be used to simulate shear response at different angles from rolling direction and the results could be compared. The overall damage to aluminum in shear has been studied by Tang et al. [2003] and revealed to be significant. The effect of ratcheting on macroscopic deformation during shear has been studied by Hassan et al. [2008]. The application of modelling equal channel angular extrusion (ECAE) using shear simulations has been studied by Kalidindi et al. [2009]. Holmedal et al. [2008] has studied the macroscopic stress strain behaviour of aluminum in different combinations of tension and compression loading conditions.

In order to expand the understanding of shear, this study compares the effect of three different strain paths predominantly containing shear. It has been shown by Mckinley et al. [2009] and Van Der Boogaard and Huetink [2006] that strain rate can affect localization and localization can be inhibited by increasing the strain rate. Strain rate effect has been studied numerically by Zikry and Nemat-Nasser [1990] for single crystal models showing a narrowing of the shear band at high strains. To investigate how pronounced an affect the strain rate has on a polycrystalline model, localization at three different strain rates are being compared in this study. Thermal softening has the opposite effect of strain rate hardening and its effect is also investigated (Lemonds and Needleman [1986]).

The paper presents computational results of strain distribution, crystallographic rotation, temperature distribution, macroscopic stress strain curves for the strain-paths studied and discusses the influence of these variables on localization.

2. Crystal Plasticity Theory

Plastic deformation of polycrystals occurs primarily by the movement of dislocations. The basic concept of dislocation was explained ingeniously by Taylor [1934] as the shearings of different rows of atoms of a crystal. First they appear in small regions, and then they begin growing through the crystal. Shear stress along the gliding direction on the gliding plane of the dislocation, known as the resolved shear stress, supplies the force to cause dislocations to glide. Among the different mechanisms of plastic deformation in metals, such as slip, twinning, grain boundary sliding and diffusion, the translation glide (slip) is the principle one in FCC metals at low and intermediate temperatures. Only this crystallographic slip mechanism is considered in this report.

Crystallographic slip is anisotropic. It implies the massive movement of dislocations along certain crystallographic planes (slip planes) in certain directions (slip directions). Each slip direction on a slip plane is called a slip system. These slip directions and planes are almost always those of maximum atomic density and correspond to those slip systems in which dislocations are most likely to move. Due to the symmetry of the crystal, there are 12 possible slip systems, $\{111\} \langle 110 \rangle$, for a FCC crystal.

The slip deformation mechanics is governed by the critical shear stress law (Schmid [1924]), which is often referred to as Schmid's law, serving as an initial microscopic yield criterion for single crystals. The Schmid law states that:

In crystals of a given material under constant condition, extensive glide occurs when the resolved shear stress, $\tau_{(\alpha)}$, attains a critical value, i.e.,

$$\tau_{(\alpha)} = r_{ij(\alpha)} \sigma_{ij} = \tau_{y(\alpha)} \quad (i, j = 1, 2, 3) \quad (1)$$

where σ_{ij} is the stress state acting on a crystal, $\tau_{y(\alpha)}$ is the yield strength of system α , and $r_{ij(\alpha)}$ is expressed as

$$r_{ij(\alpha)} = s_{i(\alpha)} m_{j(\alpha)} \quad (2)$$

where $s_{i(\alpha)}$ and $m_{j(\alpha)}$ are components of slip vector $s_{(\alpha)}$ and slip plane normal $m_{(\alpha)}$, respectively, of system α .

2.1 Single crystal deformation models

It has been known that the properties of polycrystals can be derived from those of single crystals. With the assumption that plastic deformation is due solely to crystallographic slip, the description of the deformation of single crystals has several versions. The rate-insensitive version is presented here, while the rate sensitive version is presented in Section 3.

2.1.1 Rate-insensitive deformation

Let $\tau_y^{(\alpha)}$ represent the current value of the yield stress associated with the α slip system and $\tau^{(\alpha)}$ the corresponding resolved shear stress. The Schmid law yields the following simple flow rule for rate-insensitive plasticity:

$$\dot{\gamma}_{(\alpha)} = 0 \quad \text{for } \tau_{(\alpha)} < \tau_{y(\alpha)}, \quad (3)$$

$$\dot{\gamma}_{(\alpha)} = 0 \quad \text{for } \tau_{(\alpha)} = \tau_{y(\alpha)} \text{ and } \dot{\tau}_{(\alpha)} < h_{\alpha\beta}\dot{\gamma}_{(\beta)}, \quad (4)$$

$$\dot{\gamma}_{(\alpha)} \geq 0 \quad \text{for } \tau_{(\alpha)} = \tau_{y(\alpha)} \text{ and } \dot{\tau}_{(\alpha)} = h_{\alpha\beta}\dot{\gamma}_{(\beta)}, \quad (5)$$

where $\dot{\gamma}_{(\alpha)}$ is the shear rate on slip system α , $\dot{\tau}_{(\alpha)}$ is the rate of resolved shear stress, and $h_{\alpha\beta}$ are the elements of flow stress on system α due to an increment of shear on system β .

Equations (3-5) characterises the inactive, potentially active, and active systems. The crystal deformation theory proposed by Taylor [1938] assumes that only five independent active slip systems are generally required to satisfy any arbitrary prescribed strain.

However, when deformations alone are prescribed, uniqueness is not guaranteed if more than five slip systems are potentially active. This characteristic stress and slip ambiguities in solutions of the Taylor-type models and the rate-sensitive deformation model proposed by Asaro and Needleman [1985] that resolves all these ambiguities will be discussed in detail in the next sections.

2.2 Deformation textures

The common metals of industrial practice are polycrystalline aggregates in which each grain has different orientations. In forming processes, where metals undergo medium or

large deformation, the grains in such metals do not have random orientations; instead, non-random distributions called preferred orientations or textures occur.

Textures are developed at all stages of such manufacturing processes. They have profound effects on the mechanical, thermal and electrical properties of materials, as well as on the subsequent fabrication and the final quality of products. For instance, rolling of aluminium, commercial alloys as well as high-purity materials, results in a complex mixture of a range of texture components of which are $\{112\}\langle 11\bar{1} \rangle$ (the Cu-component), $\{123\}\langle 41\bar{2} \rangle$ (the S-component), $\{110\}\langle 1\bar{1}2 \rangle$ (the brass-component) and a variety of other components. Prediction and simulation of such texture developments are very desirable, since many forming operations are carried out on rolled materials and the forming capability of metals strongly depend on their textures. Stamping a circular cup from rolled and/or annealed metal sheets with textures, for example, always results in undesirable waves on the sides of the cup, called earring.

Nevertheless, textures are so important that predicting their formation and evolution during deformation is vital for control purposes in industrial practices.

2.3 General introduction of polycrystal deformation models.

Besides the general abilities of phenomenological models, a polycrystal deformation model must have some advantages. It should be capable of describing some phenomena which cannot be covered by phenomenological theories, such as the important polycrystal deformation characteristic – crystallographic textures. It should be able to explain the resulting anisotropic material responses, such as the directional dependence of the flow stress. In general such a model can be derived from single crystal deformation models which have already included microstructures, anisotropic properties of single crystals, micromechanism (slip and/or twinning mechanisms) and lattice rotation caused by slip. The point is how microstructural mechanisms of deformation operating on the single crystal level determine polycrystal behaviours, that is how to establish a relation (reasonable, physically-based assumptions) between these two kinds of models.

To relate phenomena on the microscopic scale to those on the macroscopic scale in polycrystal plasticity theories, at least something must either be known or assumed about the stresses or strains of the individual grains. Usually, assumptions are made about the distribution of stresses and strains in the polycrystal, and polycrystal response is identified with some appropriate average of the response of its constituent grains. Several such models

have been proposed which have produced much useful insight into texture development and polycrystal strain hardening behaviour.

2.3.1 Sachs' model

Sachs' [1928] model, one of the earliest polycrystal models, was based on Sachs' original assumption that only one slip system operates in each grain. In this model, the grains are treated as if they were an array of free single crystals which can deform independently of each other. Strain and orientation changes are deduced from the stress in the same way as in the case of a free single crystal submitted to a known stress. Each grain is subjected to the same stress state which is also the macroscopic stress and is taken to be a state of uniaxial stressing. The model was refined by Kochendorfer [1941] who further stipulated that each grain was subjected to the same stretch. Then as pointed out by Bishop and Hill [1951a;1951b], with the assumption of identical strain hardening in all grains, common to the Sachs [1928] and Kochendorfer [1941] analyses, each grain fits the relation

$$\sigma/\tau = d\gamma/d\varepsilon = M \quad (6)$$

where σ and $d\varepsilon$ are the axial stress in a grain and the macroscopic aggregate strain increment respectively and τ and $d\gamma$ are the shear strength and slip system shear strain increment; M depends only on geometry and in particular on the relationship between the loading axis and the crystal slip systems. Then, as also shown by Bishop and Hill [1951a;1951b], if each grain is taken to be at the same strain hardening and if M is taken as a constant, independent of the strain, an aggregate stress strain relation can be defined as an average over all orientations, viz.

$$\sigma = \overline{M}\tau(\gamma) = \overline{M}\tau(\overline{M}\varepsilon) \quad (7)$$

The average value for \overline{M} determined by Sachs' assuming an isotropic aggregate, i.e uniform coverage of all grain orientations, is 2.2.

In Sachs' model, because of the assumption that each grain is subjected to the same stress state equal to the macroscopic stress, the stresses arising from constraints necessary to satisfy an imposed strain are neglected. As a result, continuity of stress and strain across a grain boundary is violated (Bishop and Hill [1951a;1951b]); equilibrium of the stresses cannot be established across grain boundaries; there is no way to maintain compatibility among the grains. Also some numerical inconsistencies with experiments exist in this model

(Asaro and Needleman [1985]). In general, this theory was not very successful in predicting deformation textures.

In order to overcome the objections to the Sachs' model Taylor proposed his own model. There are two aspects in the original Taylor theory: (a) a criterion for selecting the active slip systems in a deformed single crystal, for which the five components of strain rate are known, and the calculation of the remaining shear rates and rotations of the crystallographic axes; and (b) the assumptions for linking the deformation behaviour among all constituent grains, and between individual grains and polycrystals.

2.3.2 The Taylor criterion

One of Taylor's basic assumptions is that the elastic strain is neglected and the plastic strain is prescribed. Since there is essentially no change of volume for a crystal during plastic deformation, only five components of the plastic strain rate tensor are independent. The deformation model for FCC polycrystals proposed by Taylor assumes that slip from at least five independent slip systems is generally required to accommodate five independent strains. For FCC crystals which have 12 slip systems, unfortunately, there exists 384 geometrically possible combinations of 5 slip systems out of 12. His criterion for the selection of the active slip system combinations was the principle of minimum shear, which hypothesizes that among all combinations of (five) slip systems which are capable of satisfying the imposed strain, the active combination is the one for which the sum of the glide shears is a minimum, i.e.,

$$\sum_{\alpha=1}^5 \delta\gamma_{(\alpha)} = \min \quad (8)$$

This hypothesis has no obvious a priori justification. However, Taylor based it on observations of single crystals subjected to uniaxial stress and on a postulated analogy with the dynamics of non-conservative mechanical systems.

Bishop and Hill later recast the theory for polycrystals and based it on the principle of maximum work, a version of which they derived for a single crystal. In particular from the principle of maximum work, they derived inequalities between external work, computed as the product of macroscopic stress and strain increments, and internal work computed as the integral over the volumes of grains of the products of crystallographic shear strength, and assumed slip increments, and used these to set bounds on the critical stress state required to induce yield. Indeed the primary aim of the Bishop and Hill theory was the computation of single and polycrystal yield surfaces. They discovered that, for most orientations of a single crystal, the active stress states are on the corners of its yield surface. For FCC metals

deformed by $\{111\} \langle 110 \rangle$ slip and which harden isotropically, there are 56 corner stress states. More than five slip systems would be activated on these corners of the yield surface because they are the intersection of at least six planes. Among the 56 stress vertices (28 plus their opposites), 24 will activate 8 slip systems and 32 will activate 6 slip systems. Using the maximum external work rate criterion, therefore, the active slip systems can be determined rather quickly. This implies that the procedure with the Bishop and Hill theory requires considerably fewer computations than that using the Taylor theory.

The use of a yield surface in connection with “maximum plastic work” seems a more valid basis as a selection criterion than Taylor’s assumption of “minimum sum of shears”. However Chin and Mammel [1969] proved that the two methods are strictly equivalent. Kocks [1970] and Renouard and Wintenberger [1976] also arrived at the same conclusion.

2.3.3 The Taylor assumptions

The basic idea underlying the Taylor model rests on experimental observations. By examining a micrograph of the cross section of a drawn wire, Taylor noticed that all the grains were elongated in the direction of extension, and contracted in the two perpendicular directions. He concluded that the strain field throughout the polycrystals is homogeneous. This implies that each grain deforms exactly in the same way as the polycrystal. This assumption has served as a tool for linking the deformation behaviors among all constituent grains and between individual grains and polycrystals. It is known nowadays that it is not exactly true, but the assumption has the advantage of assuring continuity of the strain rate through the grain boundaries so that no voids are created.

However, with the Taylor assumption the stress state is not continuous, but varies abruptly from grain to grain, depending on different grain orientations. As pointed out by Bishop and Hill (1951a; 1951b), each grain fits the same relation as Sachs’ model (6).

Taylor and Elam [1923] studied the uniaxial tension of aluminum polycrystals. By assuming that each grain is at the same stage of strain hardening, Taylor predicted that if τ_y was the yield strength in shear of a single grain, the tensile yield stress of a random aggregate would be $3.06\tau_y$. Very close agreement was obtained when Taylor tested this theory by comparing the tensile stress-strain relation ($\sigma_{aggre.} - \epsilon$) measured on an aggregate with that deduced from the shear stress-strain ($\tau - \gamma$) curve of single crystal, where

$$\sigma_{aggre.} = \bar{M}\tau \quad (9)$$

$$\boldsymbol{\varepsilon} = \boldsymbol{\gamma} / \bar{M} \quad (10)$$

where \bar{M} , the Taylor factor, may vary from one type of texture to another. Its value is approximately 3.06 for isotropic polycrystals. We know that in the original Taylor theory, the aggregate stress is taken to be the average of the stresses generated in each grain. This concept is used in our numerical analyses to derive the macroscopic stress of a polycrystal from the stresses of constituent grains.

Summarising, two points are obtained from the Taylor theory regarding the relation between the deformation of single grains and that of polycrystals:

1. Each grain in a polycrystal experiences the same strain as the polycrystal, i.e.,

$$\boldsymbol{\varepsilon}_{\text{grain}} = \boldsymbol{\varepsilon}_{\text{aggre.}} \quad (11)$$

2. Macroscopic stress of a polycrystal is the average of the stresses of all constituent single grains, i.e.,

$$\boldsymbol{\sigma}_{\text{aggre.}} = \sum_{\text{grain}=1}^N \frac{\boldsymbol{\sigma}_{\text{grain}}}{N} \quad (12)$$

2.3.4 Relaxed constraint models

In the classical Taylor-type models, five independent slip systems have to be activated to guarantee deformation compatibility of the whole specimen. Since the number of strain conditions (the “number of constraints”) is as large as five, such models are referred to as “full constraint (FC) models”.

Recently, a modification of the Taylor model, a method of “relaxed constraints,” has been suggested by Honneff and Mecking [1978] and developed by Canova et al. [1984] to account for material texture effects. The idea here is to assume that when grains reorient and take on very distorted shapes, characterised by large aspect ratios of the principal lengths, it is possible to partially relax the strict compatibility requirements imposed in the Taylor model. Nonuniform deformations (not accounted for in the model) are envisaged to occur at the grain boundaries which accommodate the incompatibilities implied by the non-imposed strain components. When applied to certain deformation states such as axisymmetric tension and compression they argue that the dimensionality of the problem is reduced so that less than five independent slip systems are needed.

The methodology of “relaxed constraints” has been used by these authors to analyse deformation texture following several strain histories, e.g. axisymmetric tension and compression along with large simple shears in FCC polycrystals. Since the imposed strain

increments differ from those that would be imposed in a “full constraint” (Taylor) model, the slip modes and lattice rotations predicted by the two approaches are different. In a few cases the method has been reported to lead to predicted textures that are in better agreement with experiment such as in the analyses of Canova et al. [1984] of texture development following large simple shears.

2.3.5 Self-consistent schemes

The self-consistent method, based on Eshelby’s [1957] model, was proposed mainly by Kröner [1958], Budiansky and Wu [1962], and Hill [1965]. This approach attempts to account for grain interaction by considering each grain to be an ellipsoidal inclusion embedded in an infinite homogeneous matrix whose moduli are the overall moduli of the polycrystal to be determined as an average over all grains. The constraint imposed by the matrix on a grain can be estimated with the aid of Eshelby’s solution for an elastic inclusion.

This model has been argued to be the most reasonable one for simulating polycrystal plastic deformation. However, considering its rather complex mathematical aspect and the may-not-be-valid assumption of an isotropic matrix in large deformation, its limitation is obvious. Although it has successfully predicted overall strain and stress in some small and intermediate deformation cases, only few deformation textures that have been simulated by this method have been reported in the literature until now.

2.4 Discussion and Conclusion

In this section, the main deformation theories of single crystals and polycrystals have been reviewed. These deformation characteristics are the physical basis of the crystal models. They are also the physical basis of the present work.

Crystal plasticity models reviewed in this section can be classified to two groups: the self consistent models and the Taylor type models. The self-consistent models seem to be a more reasonable simulation for the plastic behaviour of polycrystals. In particular, they can account for the effects of grain shapes by choosing the ellipsoidal parameters. However, the assumption of an isotropic matrix may not be valid at large deformation. Moreover, they involve very lengthy and complex calculations for simulations of polycrystal deformation. Due to these limitations, the self-consistent models have only succeeded in being employed for the simulation of polycrystal deformation at low and intermediate strains.

Compared to the self-consistent models, the Taylor type models are simpler, and the corresponding calculation procedures are much shorter than the self consistent ones. Therefore, they have been more widely used for simulations of polycrystal deformation, particularly for predictions of texture development. The greatest disadvantage of the Taylor-type models is the violation of stress equilibrium at grain boundaries. Taylor argued that this violation could be accommodated by elastic strains. However, elastic strains are not likely to accommodate the stress differences at large strains. Further more there exist the characteristic stress and slip ambiguities in solutions of the Taylor-type models. This is because the yield surface of rate-independent single crystals is a polyhedron and the prescribed strain-rate vector must be perpendicular to the yield surface. If the prescribed strain vector is perpendicular to the edge of the yield polygon, it is not possible to determine the position of the vector on the edge. Under such conditions the stress state cannot be obtained. On the other hand, if the stress vector is on the corner of the yield locus, six or eight slip systems could possibly be simultaneously activated according to FC models, and the corresponding slips cannot be deduced uniquely. Taylor resolved this ambiguity by taking the average value of all the possible rotations. However such an average has no physical meaning. The stress and slip ambiguities are also present in solutions of RC models, although some ambiguities present in FC models may vanish because of the introduction of stress conditions.

Some postulates such as Renouard and Winterbenger [1976] and Fuh and Havner [1989] have been proposed to solve the stress and slip ambiguities. As these ambiguities cannot be resolved completely using the above two postulates, details will not be presented here. In 1985, Asaro and Needleman introduced the rate sensitivity of slip into Taylor-type crystal models to simulate the behaviour of rate-dependent polycrystals, and they thus resolved all the ambiguity problems. The characteristics of the rate-sensitive crystal plasticity model are described in Section 3 and all the simulations of crystal deformation involved in the present work are based on this model.

The Taylor-type models reviewed here have only considered the case of isotropic slip-hardening. Actually, latent hardening of slip has frequently been observed in crystal deformation. The introduction of latent hardening of slip into crystal models not only results in more realistic simulations, but also resolves the characteristic stress and slip ambiguities because different slip systems have different shear yield stresses in this situation. In Section 3, the implementation of latent hardening is described.

Unfortunately, neither the Taylor-type models nor the self-consistent models include influences of interactions of neighbouring grains. The predicted behaviour of a polycrystal is only the average of that over all grains which are considered to deform like a single crystal in the Taylor-type models or like an ellipsoidal grain surrounded by a uniform matrix. In

Section 2.5, more recent models that can incorporate the influences of individual neighbouring grains, such as grain shapes and orientations will be investigated.

2.5 New Developments in Crystal Plasticity Theory and Their Applications

New developments in the crystal plasticity theory and their applications will be examined in this section.

2.5.1 Models including interactions between grains

As will be described in Section 3, Asaro and Needleman [1985] following the pioneering work of Taylor [1938] have developed an elastic-plastic, rate dependent polycrystalline model for low homologous temperatures in which plastic deformation within the individual crystals is taken to be by crystallographic slip alone. This model assumes that all grains have equal volume, and that the deformation gradient within each grain has a uniform value throughout the aggregate. As discussed before, in this model, compatibility is satisfied and equilibrium holds in each grain. However, the deformation producing mechanisms of twinning, diffusion and grain boundary sliding are not considered, and other sources of anisotropy due to morphological effects of grain shape, size and arrangement are not taken into account.

If grain shape effects are not included, the predicted textures are not in good agreement with experimental textures. In particular, if the Taylor assumption is used to model the texture development of an aggregate whose grains have become flat and elongated, the major texture components are shifted in Euler space and the minor texture components are incorrect.

Asaro and co-workers (i.e., Harren et al. [1988]) have conducted some novel experiments and simulations of shear band formation in Al-3wt% Cu FCC single and polycrystals under plane strain compression. In their work, they modelled each grain by a number of finite elements to allow for non-uniform deformations within the grains, and in their calculations compatibility and equilibrium within and between grains was satisfied by the finite element method. Their simulations of the deformation response of a multi-crystal comprising of 27 grains provided good insight into the underlying micromechanical mechanisms of localised deformation in crystalline materials.

Mathur et al. [1990] extended the mathematical formulation developed earlier by Mathur and Dawson [1989] to account for the effects of grain shape on the development of

deformation-induced crystallographic texture using the relaxed constraints approach of Honneff and Mecking [1978] and Kocks and coworkers (Kocks and Canova [1981], Canova et al. [1984], Tomé et al. [1984]). Within their framework, each grain could no longer be treated independently and the stresses from all grains in an aggregate simply be averaged. Rather, in a restricted sense the actual continuity requirements from continuum mechanics were enforced across flat grain boundaries while the overall deformation of an aggregate is constrained to match the macroscopic deformation of the material point. They simulated the flat rolling of polycrystalline aluminum as an application for their model and compared the predicted deformation textures with the predictions of an earlier study which were based on a Taylor model. Several detailed comparisons indicated that the texture predictions made by the new model which accounts for morphological effects matched the experimental observations more closely.

Kalidindi et al. [1992] developed a finite element polycrystalline model where the integration point represents a material point in a single grain and the constitutive response is given through a single-crystal model without invoking the Taylor assumption. In their numerical simulations, each element represented one crystal, and sets of initially “random” grain orientations had been assigned to the elements. As with Taylor model simulations, the macroscopic stress-strain response and crystallographic texture were computed as volume averages over the entire aggregate. The crystallographic texture was arrived at by direct equal-area projection of the orientations of all grains. Their calculations satisfied (in the “weak” finite element sense) both compatibility and equilibrium in the aggregate. They analysed FCC polycrystalline oxygen-free-high-conductivity (OFHC) copper for (i) planar simple shear and thin-walled tubular torsion to large shear strains, and (ii) a simple plane-strain forging operation. Their results clearly indicated that the new model nicely captured the major features of the evolved texture.

Bronkhorst et al. [1992] used this model to simulate “nominally homogeneous” deformations of simple compression and tension, plane strain compression, and simple shear of a polycrystalline aggregate by using a multitude of single crystals. They compared their results against results from Taylor-type calculations and concluded that their model was in much better agreement with the experiments than that was the Taylor-type model, but at a substantially higher computational expense.

Anand and Kalidindi [1994] also used this model to simulate the effects of crystallographic texture evolution on the process of shear band formation in plane strain compression of initially isotropic OFHC polycrystalline copper. They have calculated texture that is in very good qualitative agreement with the experimental texture after an axial compressive strain of -1.0 .

The study of a model polycrystal using finite element simulations (Sarma and Dawson [1996a]) showed neighbour interactions to be the main factor in determining the spread of the applied deformation among the crystals. Sarma and Dawson [1996b] presented a viscoplastic model for distributing the deformation applied to a polycrystal in a non-uniform fashion among the constituent crystals. Their finite element model was based on the hybrid formulation of Beaudoin et al. [1995] in which compatibility was accomplished through interelement continuity of the velocity field and equilibrium was satisfied identically within the elements through the choice of interpolation functions and across element boundaries via a weighted residual. By defining a local neighbourhood for each crystal in this model, the effect of neighbour interactions were incorporated in this model for partitioning the macroscopic deformation. They computed a compliance tensor for each crystal based on a viscoplastic constitutive relation for deformation by crystallographic slip. Since they used the Taylor model for calculating the compliance of each crystal, the new model may be viewed as a modification of the Taylor hypothesis, using an equilibrium based approach at the level of the neighbourhood of each crystal. The compliance of the crystal relative to that of its neighbourhood provided a means for partitioning the macroscopic deformation rate among the crystals. Polycrystal simulations of crystallographic texture development under plane strain compression and simple shear were simulated with this model and the results obtained were compared to the results of similar calculations using a Taylor model. They concluded that the model incorporating neighbour interactions improved texture predictions, in terms of both the intensity levels and the locations of certain texture components.

2.5.2 Strain gradient plasticity

Dislocation theory suggests that the plastic flow strength of a solid depends on strain gradients in addition to strains. Hardening is due to the combined presence of geometrically necessary dislocations associated with a plastic strain gradient and statistically stored dislocations associated with plastic strain. In general, strain gradients are inversely proportional to the length scale over which plastic deformation occurs. Thus, gradient effects become important for plastic deformations taking place at small scales. Experimental evidence suggests that flow strength increases with diminishing size, at length scales on the order of several microns or less.

The most general versions of the theories proposed fit within the Toupin-Mindlin strain gradient framework, which involves all components of the strain gradient tensor and work-conjugate higher-order stresses in the form of couple stresses and double stresses. A specialized version deals with only a subset of the strain gradient tensor in the form of deformation curvatures (i.e., rotation gradients); this is the simpler couple stress framework.

Experimental evidence is accruing for the existence of a strong size effect in the plastic flow of metals and ceramics. For example, the measured indentation hardness of metals and ceramics increases by a factor of about two as the width of the indent is decreased from about 10 μm to 1 μm (Stelmashenko et al. [1993], Ma and Clarke [1995]). The well-known Hall-Petch effect states that the yield strength of pure metals increases with diminishing grain size. Long-standing observations of shear bands in metals have revealed that micro-shear band widths appear to be consistently on the order of a micron. Simple dimensional arguments lead to the conclusion that any continuum theory for each of these phenomena based solely on strain hardening, with no strain gradient dependence, would necessarily predict an absence of any such size effect.

Higher-order continuum theories of elasticity were promulgated in the 1960s culminating with the major contributions of Koiter [1964], Mindlin [1964, 1965] and Toupin [1962]. Efforts were made to apply the theories to predict phenomena for linear elastic solids such as stress concentration at holes (Mindlin [1963]), crack-tip stresses (Eringen [1968]), bending stiffness of thin beams (Koiter [1964]), and stresses at free surfaces (Mindlin [1965]). No experimental corroboration of these theories was achieved, and in due course it was generally accepted that the phenomena being addressed in these works should be expected to come into play only at scales comparable to atomic lattice spacing. Specifically, Koiter's [1964] argument prevailed to the effect that there is no reason to expect gradient effects to alter the elastic bending stiffness of a single crystal beam until its thickness approaches atomic dimensions. Fleck and Hutchinson [1993] have developed a phenomenological theory of strain gradient plasticity based on gradients of rotation which fits with the framework of couple stress theory. This theory is probably the simplest generalization of conventional isotropic-hardening plasticity theory to include strain gradient effects.

There have been several studies with the aim of providing higher-order strain gradient constitutive relations for conventional linear elastic solids with microstructures (i.e., Zuiker and Dvorak [1994], Drugan and Willis [1996] for materials reinforced by spherical particles, and Bardenhagen and Triantafyllidis [1996] for multi-phase media). Complementing this theoretical work are the experiments by Kakunai et al. [1985] on polycrystalline aluminum beams with equiaxed grains showing a small but systematic increase in the scaled elastic-bending stiffness as the thickness of the beams is reduced from about sixty to three grain diameters.

While gradient effects in an elastic single crystal of pure metal become significant only for deformation fields with wavelengths on the order of the atomic spacing, when plastic deformation occurs, gradient effects can become important at much larger scales.

Fleck and Hutchinson [1997] used the notions of statistically stored dislocations and geometrically necessary dislocations to provide the physical basis for continuum theory of single-crystal plasticity. They assumed that slip occurs on specific slip systems in a continuous manner and the increment in flow strength of any given slip system depends upon the rates of both the strain and the first spatial gradient of strain. Their crystal theory fits within the framework of Toupin [1962] and Mindlin [1964,1965] strain gradient theory. It should be mentioned that the precise details of the formulation that incorporates strain gradients to crystal plasticity are not yet clear but are being pursued.

2.5.3 Models including backstress

Polycrystalline plasticity formulations to date have neglected explicit effects of dislocation substructure in the constitutive relations. As a result, aphysical symptoms arise such as premature texture development (Harren et al. [1989]).

When a metal deforms inelastically, heterogeneities arise due to mechanisms at several length scales. These heterogeneities can arise from single dislocation sources at the lattice or at a higher length scale via dislocation cell boundaries enclosing equiaxed volumes that contain few dislocations. Heterogeneities can also arise at higher length scales from geometrically necessary boundaries (GNBs) which surround groups of cells in cell blocks (CBs) (Kuhlmann-Wilsdorf [1989], Leffers [1992]). Heterogeneities give arise to internal stresses associated with local hard and soft regions; hence, macroscale hardening behaviour during inelastic deformation ensues from dislocations simultaneously interacting throughout a range of length scales. These heterogeneities not only generate short range stresses at a local level which induce anisotropy but also affect the polycrystalline elastic anisotropy.

The crystal plasticity models that have been already discussed have been successful in predicting the elasto-plastic behaviour as well as the texture evolution of crystalline materials. However, the backstress evolution has been neglected in these models. The backstress is a residual stress embedded in the polycrystalline or single crystal material at the crystal-lattice level due to plastic deformation of crystals.

Within the context of dislocation resistance, the notion of backstress was studied by Mughrabi [1983]. It has been used in some plasticity models to describe the Bauschinger effect which has been associated with sequential activation, deactivation, and dislocation substructures. The backstress arises as dislocation densities at the GNBs are high enough to induce a tensile stress state (or forward stress) such that regions between them experience a compressive stress state. To maintain compatibility at the interface between the boundaries and interiors of the subgrain, the GNBs serve as barriers to dislocation motion and give rise

to backstress. These backstresses influence the work-hardening rate and limit the free operation of dislocation sources in the softer cell interiors when the material is reloaded. Tensile stresses (or forward stresses) in the boundaries assist the applied stresses to operate on the sources with shorter dislocation segments.

Horstemeyer and McDowell [1998] introduced a second rank microheterogeneity internal state variable (ISV) tensor into the elastoviscoplastic polycrystalline framework (Rashid and Nemat-Nasser [1990]) to represent effects of dislocation substructures in the form of geometrically necessary boundaries (GNBs). This evolving ISV was resolved onto the slip systems using Schmid's Law to introduce kinematic hardening (backstress) in the flow rule. The microheterogeneity ISV tensor that they introduced also affected the intergranular constraint by using a self-consistent (relaxed constraint) method analogous to that of Berveiller and Zaoui [1978]. This microheterogeneity ISV relates the dislocation substructure evolution to the backstress for intergranular hardening and to the grain boundaries for intergranular hardening. By including the microheterogeneity ISV into the elastoviscoplastic polycrystalline framework relative to the Taylor model they improved trends of correlations with experimental compression and torsion stress-strain curves. Also the trends of their prediction of axial stresses in fixed end torsion tests were more realistically simulated as second order axial effects were shown to depend on both texture and dislocation substructure. Two other noteworthy results they presented were that the trends of intensity and distribution (spread) of texture evolution were more realistically predicted and that the trends of prediction of polycrystalline elastic moduli for deformed OFHC Cu and 304L stainless steel were more accurately simulated. Also their elastoviscoplastic calculations with the microheterogeneity ISV model showed that torsion produced a higher degree of anisotropy than compression since the backstress magnitude for torsion was greater than for compression. Their results and also other results such as presented by Voyiadjis and Huang [1996] and Dawson et al. [1999] suggest that residual stresses such as backstress and their evolutions should be considered for a physically-based polycrystalline framework.

Brahme et al. [2009] integrated the approach proposed by Berveiller and Zaoui [1978] into a polycrystalline model to establish the amount of backstress due to cell block boundaries (CBBs). It was shown that the addition of backstress into the model altered the activity on some of the slip systems and in turn, increased the localization predicted as well as altered the evolved texture.

2.5.4 Discrete dislocation plasticity

It has already been discussed that conventional plasticity theories are length-scale independent and are based on the concept of a homogeneously deformed material element.

However based on crystal plasticity, Van Der Giessen and Needleman [1995] have presented a method for solving small-strain plasticity problems with plastic flow represented by the collective motion of a large number of discrete dislocations.

Their formulation assumed that the ensuing deformation process was quasi-static and involved small strains only. The process lead to the motion of dislocations, mutual annihilation, the generation of new dislocations and their pinning at point obstacles. The analysis of the deformation process was performed in an incremental manner in time, where the incremental step at any instant t involves three main computational stages. First, for the current dislocation arrangement, the current stress and strain state of the problem was determined. Secondly, from that state, the so-called Peach-Koehler force, i.e., the driving force for changes in the dislocation structure, was determined. Finally, the instantaneous rate of that dislocation structure was computed on the basis of a set of constitutive equations for motion, annihilation and generation of dislocations.

They have presented results for monophasic and composite materials with periodic microstructures subjected to simple shear loading. Even though they were only for a single slip system and use assumptions for sources and obstacles, the results showed a number of noteworthy features; especially in problems of plastic flow near crack tips, around micro-indentors and in composite materials, at a scale where the collective motion of large numbers of dislocations and discrete dislocation effects play a role. Their results indicated that for the aforementioned microscale problems, continuum plasticity may not give the desired resolution of stress and strain fields on that scale, and that the discrete nature of dislocations may need to be accounted for.

3. Constitutive Model

The polycrystal plasticity model formulated by Asaro and Needleman [1985] and used by Inal et al. [2002a] is employed in this analysis. The total deformation of a crystallite is taken to be the result of two distinct physical mechanisms: crystallographic slip due to dislocation motion on the active slip systems, and elastic lattice distortion. Within an FCC crystal, plastic deformation occurs by crystallographic slip on the twelve $\{111\}\langle 110 \rangle$ slip systems where the slip planes are the $\{111\}$ crystallographic planes with normals \mathbf{m} , and the $\langle 110 \rangle$ directions are the shear directions with slip vectors \mathbf{s} . Plastic deformation is envisaged to occur as a set of plastic simple shears along the various slip systems, leaving the lattice and the slip system vectors ($\mathbf{s}_{(\alpha)}, \mathbf{m}_{(\alpha)}$) not only essentially undistorted, but also unrotated. (The brackets for the subscripts α indicate that α is not a tensor index and ranges from one to the total number of slip systems.) Next, the material and lattice are considered to deform elastically and rotate rigidly from the plastically deformed state to the current configuration (Figure 1).

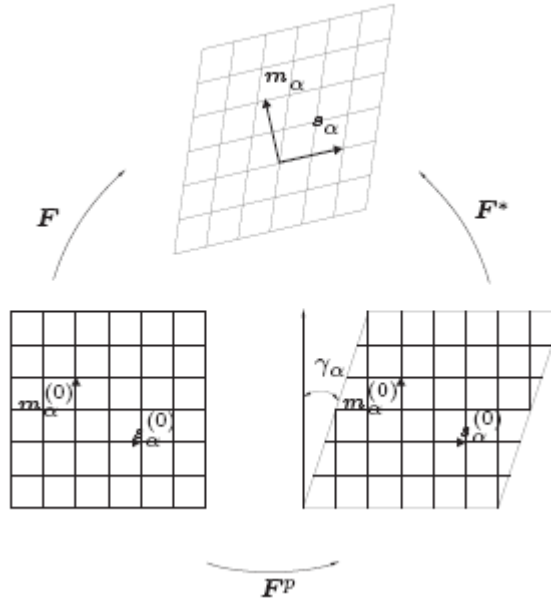


Figure 1: Decomposition of the deformation gradient F .

Accordingly, the deformation gradient tensor F is written as:

$$F = F^* F^p, \quad (13)$$

where \mathbf{F}^p consists solely of crystallographic slip along the specific slip systems, while the elastic deformation and any rigid body rotation are embodied in \mathbf{F}^* . From (13), the spatial gradient of velocity \mathbf{L} can be written as

$$\mathbf{L} = \dot{\mathbf{F}}\mathbf{F}^{-1} = \mathbf{L}^* + \mathbf{L}^p, \quad (14)$$

where

$$\mathbf{L}^* = \dot{\mathbf{F}}^* \mathbf{F}^{*-1}, \quad \mathbf{L}^p = \mathbf{F}^* (\dot{\mathbf{F}}^p \mathbf{F}^{p-1}) \mathbf{F}^{*-1} \quad (15)$$

Taking symmetric and antisymmetric parts of the above relations leads to the elastic and plastic strain-rates \mathbf{D}^* and \mathbf{D}^p , the so-called plastic spin \mathbf{W}^p , and the spin \mathbf{W}^* associated with the rigid lattice rotation

$$\mathbf{D} = \mathbf{D}^* + \mathbf{D}^p, \quad \mathbf{W} = \mathbf{W}^* + \mathbf{W}^p \quad (16)$$

The vectors $s_{(\alpha)}$ and $m_{(\alpha)}$ are regarded as lattice vectors so that they stretch and rotate by

$$s_{(\alpha)}^* = \mathbf{F}^* s_{(\alpha)}, \quad m_{(\alpha)}^* = m_{(\alpha)} \mathbf{F}^{*-1} \quad (17)$$

By introducing the following symmetric and skew-symmetric tensors for each slip system α ,

$$\mathbf{P}_{(\alpha)} = \frac{1}{2} [s_{(\alpha)}^* \otimes m_{(\alpha)}^* + m_{(\alpha)}^* \otimes s_{(\alpha)}^*] \quad (18)$$

$$\mathbf{W}_{(\alpha)} = \frac{1}{2} [s_{(\alpha)}^* \otimes m_{(\alpha)}^* - m_{(\alpha)}^* \otimes s_{(\alpha)}^*], \quad (19)$$

the plastic strain-rate and spin for the crystal can be respectively written as

$$\mathbf{D}^p = \sum_{\alpha} \mathbf{P}_{(\alpha)} \dot{\gamma}_{(\alpha)}, \quad \mathbf{W}^p = \sum_{\alpha} \mathbf{W}_{(\alpha)} \dot{\gamma}_{(\alpha)} \quad (20)$$

where $\dot{\gamma}_{(\alpha)}$ is the shear rate on the slip system α .

The elastic constitutive equation for a crystal is specified by

$$\overset{\nabla}{\boldsymbol{\tau}}^* = \dot{\boldsymbol{\tau}} - \mathbf{W}^* \boldsymbol{\tau} + \boldsymbol{\tau} \mathbf{W}^* = \mathbf{L} \mathbf{D}^* \quad (21)$$

where $\overset{\nabla}{\boldsymbol{\tau}}^*$ is the Jaumann rate of the Kirchhoff stress tensor $\boldsymbol{\tau}$ based on the lattice rotations, and \mathbf{L} is the tensor of the elastic moduli. These moduli are based on the anisotropic elastic constants of the FCC crystals and thus exhibit the appropriate cubic symmetry.

In order to express the constitutive equation (21) in terms of the Jaumann rate $\overset{\nabla}{\boldsymbol{\sigma}}$ of the Cauchy stress $\boldsymbol{\sigma} = \det(\mathbf{F})^{-1} \boldsymbol{\tau}$ based on the continuum slip \mathbf{W} , we introduce a second-order tensor $\mathbf{R}_{(\alpha)}$ for each slip system as follows

$$\mathbf{R}_{(\alpha)} = \mathbf{L} \mathbf{P}_{(\alpha)} + \mathbf{W}_{(\alpha)} \boldsymbol{\sigma} - \boldsymbol{\sigma} \mathbf{W}_{(\alpha)} \quad (22)$$

Using (16) – (20) and (22), the constitutive equation (21) can be rewritten in the form

$$\overset{\nabla}{\boldsymbol{\sigma}} = \mathbf{L} \mathbf{D} - \dot{\boldsymbol{\sigma}}^0 - \boldsymbol{\sigma} \text{tr} \mathbf{D} \quad (23)$$

where $\dot{\boldsymbol{\sigma}}^0$ is a viscoplastic type stress-rate defined by

$$\dot{\boldsymbol{\sigma}}^0 = \sum_{\alpha} \mathbf{R}_{(\alpha)} \dot{\gamma}_{(\alpha)} \quad (24)$$

The slip rates to be substituted into equation (24) are assumed to be governed by the following power-law expression

$$\dot{\gamma}_{(\alpha)} = \dot{\gamma}_{(0)} \text{sgn} \tau_{(\alpha)} \left| \frac{\tau_{(\alpha)}}{g_{(\alpha)}} \right|^{1/m} \quad (25)$$

Here $\dot{\gamma}_{(0)}$ is a reference shear rate taken to be the same for all the slip systems, $\tau_{(\alpha)} = \mathbf{P}_{(\alpha)} : \boldsymbol{\sigma}$ is the resolved shear stress on slip system α , $g_{(\alpha)}$ is its hardness and m is the strain-rate sensitivity index. The functions $g_{(\alpha)}$ characterize the current strain-hardened state of all slip systems. The rate of increase of the function $\dot{g}_{(\alpha)}$ is defined by the hardening law:

$$\dot{g}_{(\alpha)} = \sum_{\beta} h_{(\alpha\beta)} \left| \dot{\gamma}_{(\beta)} \right| \quad (26)$$

where $g_{(\alpha)}(0)$ is the initial hardness, taken to be a constant τ_0 for each slip system, and $h_{(\alpha\beta)}$ are the hardening moduli. The form of these moduli is

$$h_{(\alpha\beta)} = q_{(\alpha\beta)} h_{(\beta)} \quad (\text{no sum on } \beta) \quad (27)$$

where $h_{(\beta)}$ is a single slip hardening rate, and $q_{(\alpha\beta)}$ is the matrix describing the latent hardening behaviour of the crystallite. For FCC crystals with 12 slip systems, we take $q_{(\alpha\beta)}$, as in Asaro and Needleman [1985], to be given by

$$q_{(\alpha\beta)} = \begin{bmatrix} A & qA & qA & qA \\ qA & A & qA & qA \\ qA & qA & A & qA \\ qA & qA & qA & A \end{bmatrix} \quad (28)$$

where q is the ratio of the latent hardening rate to self hardening rate, and A is a 3 x 3 matrix fully populated by ones. In the above, slip systems $\{1,2,3\}$ are coplanar, as are systems $\{4,5,6\}$, $\{7,8,9\}$ and $\{10,11,12\}$. Thus the ratio of the latent hardening rate to the self hardening rate for coplanar systems are taken as unity.

Asaro and Needleman [1985], among others, simply take each $g_{(\alpha)}$ to depend on the accumulated sum γ_a of the slips; i.e.,

$$g_{(\alpha)} = g_{(\alpha)}(\gamma_a), \quad \gamma_a = \int_0^t \sum_{\alpha} |\dot{\gamma}_{(\alpha)}| dt \quad (29)$$

Peirce et al. [1982] take the slip hardening to be a function of γ_a , the total slip on all of the systems:

$$h_{(\beta)} = h_0 \left(\frac{h_0 \gamma_a}{\tau_0 n} + 1 \right)^{(n-1)} \quad (30)$$

where h_0 is a hardening constant, n is the hardening exponent, and τ_0 is the critical resolved shear stress.

It has been discussed in Section 2 that neither the Taylor model nor the self consistent models can resolve the problem of nonuniqueness in the choice of active slip systems. In a rate dependent formulation, such as what has just been described in Section 3, there is no division of slip systems into “active” or “inactive” sets. Instead all slip systems always slip at a rate which depends on the current stress and hardness properties. In equations (25) and (26), we use a simple power law relation between the slipping rate on a slip system and the ratio of resolved shear stress to a hardness parameter. The hardening parameter evolves with strain (equation (26)) according to a law which describes both self hardening and latent hardening of the slip systems. Thus once the stress state is known, which it is in the context of the model, slipping rates on all possible slip systems and the resulting lattice rotations are uniquely determined.

3.1 Orientation Update

For each time step, once \mathbf{W}^* is known, the orientation of the crystal is updated by updating the orientation matrix. The orientation matrix, \mathbf{Q} , rotates the crystal axis into the lab system, and is updated using the method of Raphanel et al. [2004].

$$\mathbf{Q}_{n+1} = e^{\mathbf{W}^* \Delta t} \mathbf{Q}_n \quad (31)$$

$\exp(\mathbf{W}^* \Delta t)$ is obtained through the Euler-Rodrigues formula

$$e^{\mathbf{W}^* \Delta t} = \mathbf{I} + \frac{\sin w^* \Delta t}{w^*} \mathbf{W}^* + \frac{1 - \cos w^* \Delta t}{(w^*)^2} \mathbf{W}^* \mathbf{W}^* \quad (32)$$

where $w^* = \sqrt{(\mathbf{W}_{ij}^* \mathbf{W}_{ij}^*)/2}$.

From the updated orientation matrix, the Euler angles (ϕ_1, ϕ, ϕ_2) in Bunge’s notation are computed and stored. These Euler angles are used to track the evolution of the texture of the material in polycrystal calculations (Kocks et al., [2001]).

4. Numerical Implementation

In this section, the implementation of the crystal plasticity code into the explicit FE solver is discussed. A forward euler time integration is proposed and compared with a rate tangent method. The construction of the microstructure model and the finite element mesh is also discussed.

4.1 Time Integration methods

4.1.1 Rate tangent modulus method

Here, we briefly summarize the semi-implicit, forward-gradient time-integration procedure developed by Peirce et al. [1983,1984] which we use in our simulation. Considering the slip-rate law expressed in equation (25), the slip increment on system α at time t is given by

$$\Delta\gamma^{(\alpha)} = \gamma^{(\alpha)}(t + \Delta t) - \gamma^{(\alpha)}(t) \quad (33)$$

A linear interpolation is employed within the time increment to give

$$\Delta\gamma^{(\alpha)} = \left[(1 - \theta)\dot{\gamma}^{(\alpha)}(t) + \theta\dot{\gamma}^{(\alpha)}_{(t+\Delta t)} \right] \Delta t \quad (34)$$

where Δt is the time increment. Finally, the slip increments, according to equation (34), can be expressed in terms of the quantities at time t as

$$\Delta\gamma^{(\alpha)} = (\dot{\mathbf{f}}^{(\alpha)} + \mathbf{F}^{(\alpha)} : \mathbf{D})\Delta t \quad (35)$$

where

$$\dot{\mathbf{f}}^{(\alpha)} = \sum_{\beta} \mathbf{M}_{\alpha\beta} \dot{\gamma}_t^{(\alpha)}, \quad \dot{\mathbf{F}}^{(\alpha)} = \sum_{\beta} \mathbf{M}_{\alpha\beta} \mathbf{Q}^{(\alpha)}, \quad \text{and} \quad \mathbf{Q}^{(\alpha)} = \left(\frac{\theta \Delta t \dot{\gamma}_t^{(\alpha)}}{m \tau^{(\alpha)}} \right) \mathbf{R}^{(\alpha)} \quad (36)$$

Here, $\mathbf{M}_{\alpha\beta}$ is the inverse of matrix $N_{\alpha\beta}$ defined by

$$N_{\alpha\beta} = \delta_{\alpha\beta} + \left(\frac{\theta \Delta t \dot{\gamma}_t^{(\alpha)}}{m} \right) x \left[\frac{\mathbf{R}^{(\alpha)} : \mathbf{P}^{(\beta)}}{\tau^{(\alpha)}} + \text{sgn}(\tau^{(\beta)}) \frac{h_{\alpha\beta}}{g^{(\alpha)}} \right] \quad (37)$$

4.1.2 Forward Euler Algorithm

In this section, the proposed forward Euler algorithm in the subroutine is presented. The basic idea behind this algorithm is to use the slip rates per slip system at time $t_{(n)}$ to compute quantities for time $t_{(n+1)}$. In step 4 below, for example, $\dot{\gamma}_{\alpha}^{(n)}$ is used to compute plastic spin, plastic part of the plastic strain rate and the \mathbf{R} tensor. Likewise, in steps 5 and 6, we use plastic slip rates from $t_{(n)}$ to compute slip plasticity related quantities for time $t_{(n+1)}$.

The steps in the computation are as follows:

- (1) Subroutine entry with known values of $\mathbf{F}_{(n+1)}$, $\mathbf{F}_{(n)}$, $\mathbf{P}_{\alpha}^{(n)}$, $\mathbf{W}_{\alpha}^{(n)}$, $\boldsymbol{\sigma}_{(n)}$, and Dt
- (2) Compute deformation and spin variables for $t_{(n+1)}$

$$\begin{aligned}\dot{\mathbf{F}}_{(n+1)} &= \frac{\mathbf{F}_{(n+1)} - \mathbf{F}_{(n)}}{\Delta t} \\ \mathbf{L}_{(n+1)} &= \dot{\mathbf{F}}_{(n+1)} \mathbf{F}_{(n+1)}^{-1} \\ \mathbf{D}_{(n+1)} &= \text{sym}(\mathbf{L}_{(n+1)}) \\ \mathbf{W}_{(n+1)} &= \text{skew}(\mathbf{L}_{(n+1)})\end{aligned}$$

- (3) Approximate the slip shear rates for $t_{(n+1)}$ using the stress state and $\mathbf{P}_{\alpha}^{(n)}$ at time $t_{(n)}$.

$$\begin{aligned}\tau_{\alpha}^{(n)} &= \mathbf{P}_{\alpha}^{(n)} : \boldsymbol{\sigma}_{(n)} \\ \dot{\gamma}_{(\alpha)} &= \dot{\gamma}_{(0)} \text{sgn} \tau_{(\alpha)} \left| \frac{\tau_{(\alpha)}}{\mathcal{G}_{(\alpha)}} \right|^{1/m}\end{aligned}$$

- (4) Use slip shear rates to compute plastic strain rate and plastic spin.

$$\begin{aligned}\mathbf{D}_{(n)}^p &= \sum_{\alpha} \mathbf{P}_{(\alpha)}^{(n)} \dot{\gamma}_{(\alpha)}^{(n)} \\ \mathbf{W}_{(n)}^p &= \sum_{\alpha} \mathbf{W}_{(\alpha)}^{(n)} \dot{\gamma}_{(\alpha)}^{(n)} \\ \mathbf{R}_{\alpha}^{(n)} &= \mathbf{L}_{(n)} \mathbf{P}_{\alpha}^{(n)} + \mathbf{W}_{\alpha}^{(n)} \boldsymbol{\sigma}_{(n)} - \boldsymbol{\sigma}_{(n)} \mathbf{W}_{\alpha}^{(n)}\end{aligned}$$

- (5) Compute visco-plastic stress rate, Jaumann rate of Cauchy stress for $t_{(n+1)}$ and update Cauchy stress.

$$\dot{\sigma}_{(n)}^0 = \sum_{\alpha} R_{\alpha}^{(n)} \dot{\gamma}_{\alpha}^{(n)}$$

$$\overset{\nabla}{\mathbf{L}}_{(n+1)} = \mathbf{L}_{(n)} \mathbf{D}_{(n+1)} - \dot{\sigma}_{(n)}^0 - \sigma_{(n)} \text{tr} \mathbf{D}_{(n+1)}$$

$$\sigma_{(n+1)} = \sigma_{(n)} + \left(\overset{\nabla}{\sigma}_{(n+1)} + \mathbf{W}_{(n+1)} \sigma_{(n)} - \sigma_{(n)} \mathbf{W}_{(n+1)} \right) \Delta t$$

(6) Compute the plastic portion of the deformation gradient, \mathbf{F}^* and \mathbf{W}^* .

$$\mathbf{F}_{(n)}^p = \mathbf{I} + \sum_{\alpha} \dot{\gamma}_{\alpha}^{(n)} s_{\alpha}^{(n)} \otimes m_{\alpha}^{(n)}$$

$$\mathbf{F}_{(n+1)}^* = \mathbf{F}_{(n+1)} \mathbf{F}_{(n)}^{p-1}$$

$$\mathbf{W}_{(n+1)}^* = \mathbf{W}_{(n+1)} \mathbf{W}_{(n)}^p$$

(7) Compute $\exp(\mathbf{W}_{(n+1)}^* \Delta t) \mathbf{Q}_{(n)}$ using the Euler-Rodrigues formula and update the orientation matrix using $\mathbf{Q}_{(n+1)} = (\mathbf{W}_{(n+1)}^* \Delta t) \mathbf{Q}_{(n)}$.

(8) Compute Euler angles; rotate the crystallite modulus and lattice vectors and compute $\mathbf{P}_{(\alpha)}$ and $\mathbf{W}_{(\alpha)}$ tensors.

$$\mathbf{Q}_{(n+1)} \longrightarrow \phi_1^{(n+1)}, \phi_2^{(n+1)}, \phi_3^{(n+1)}$$

$$\mathbf{L}_{(n+1)}^0 = \mathbf{Q}_{(n+1)} \mathbf{Q}_{(n+1)} \mathbf{L}_{(0)}^0 \mathbf{Q}_{(n+1)}^T \mathbf{Q}_{(n+1)}^T$$

$$s_{(\alpha)}^{*(n+1)} = \mathbf{F}_{(n+1)}^* \mathbf{Q}_{(n+1)} s_{(\alpha)}$$

$$m_{(\alpha)}^{*(n+1)} = \mathbf{F}_{(n+1)}^{*-I} \mathbf{Q}_{(n+1)} m_{(\alpha)}$$

$$\mathbf{P}_{\alpha}^{(n+1)} = \frac{1}{2} \left[s_{(\alpha)}^{*(n+1)} \otimes m_{(\alpha)}^{*(n+1)} + m_{(\alpha)}^{*(n+1)} \otimes s_{(\alpha)}^{*(n+1)} \right]$$

$$\mathbf{W}_{\alpha}^{(n+1)} = \frac{1}{2} \left[s_{(\alpha)}^{*(n+1)} \otimes m_{(\alpha)}^{*(n+1)} - m_{(\alpha)}^{*(n+1)} \otimes s_{(\alpha)}^{*(n+1)} \right]$$

(9) Compute total slip, hardening and update the shear strengths of the slip systems.

$$\gamma_{\alpha}^{(n+1)} = \gamma_{\alpha}^{(n)} + \sum_{\alpha} |\dot{\gamma}_{\alpha}^{(n)}| \Delta t$$

$$h(\gamma^{(n+1)}) = h_0 \text{sech}^2 \left(\frac{h_0 \gamma_{\alpha}^n}{g_s - g_0} \right)$$

$$g_{\alpha}^{(n+1)} = g_{\alpha}^{(n)} + \sum_{\beta} h_{\alpha\beta}^{(n+1)} \left| \dot{\gamma}_{\beta}^{(n)} \right| \Delta t$$

(10) Exit subroutine.

4.1.3 Validation of the Forward Euler Algorithm

First we validate our forward Euler algorithm by carrying out single element (which represents a single crystal) computations. Single element calculations carried out by Raphanel et al. [2004] were repeated using the forward Euler scheme and the results are compared with those obtained by them. Model parameters used in this crystal plasticity simulation are taken from the preceding reference and are shown in Table 1. The rate of loading was 0.001/s for all runs.

Table 1: Material Parameters Used in the Simulations.

Property	$\dot{\gamma}$	h_0 / τ_0	m	q	ν	τ_0	E
Value	0.001 1/s	8.9	0.02	1 or 1.4	0.3	1 MPa	1

Figure 2 presents results of single element computations where loading directions were uniaxial and in the [100] and $[\bar{1}11]$ directions. The results from the forward Euler algorithm are shown as solid lines and these results are compared with those of Raphanel et al. [2004] for the same loading directions, shown as dashed lines. It can be seen that the explicit forward Euler scheme used in an explicit code gives results that are identical to those obtained with the second order Runge-Kutta scheme used in an implicit code. Onset of yielding for the [100] direction is when $\sigma/\tau_0 = \sqrt{6}$ and this is in accord with the rigid plastic theory of Taylor, Bishop and Hill (Hosford, [1993]). In the case of the results of the $[\bar{1}11]$ loading, yielding occurs at $3\sqrt{3}/\sqrt{2}$, which is also in accord with theory. It is worth noting that in these calculations $q = 1$ and latent hardening does not play a role for these loading directions.

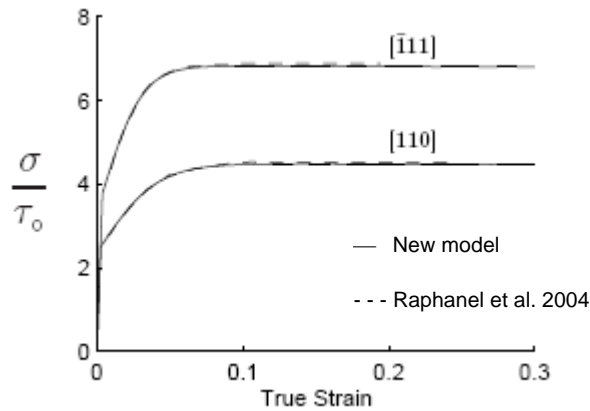


Figure 2: Stress strain curves for uniaxial loading in [001], and [-111] directions.

Figure 3 presents single element computations for uniaxial loading in the $[-123]$ direction where the transverse and normal directions were $[54-1]$ and $[1-11]$, respectively. Here, the effect of slip system rotation and therefore the effects of latent hardening are examined. Note that parameter q controls the magnitude of latent hardening; $q = 1$ corresponds to isotropic hardening while $q = 1.4$ corresponds to latent hardening. Irrespective of the hardening case, the loading direction considered here is inherently unstable and the slip systems rotate to take the crystal to a stable orientation. The stress-strain curves for this direction for both $q = 1$ and $q = 1.4$ are shown in Figure 3, showing that latent hardening plays a significant role in deciding the shape of the stress-strain curve.

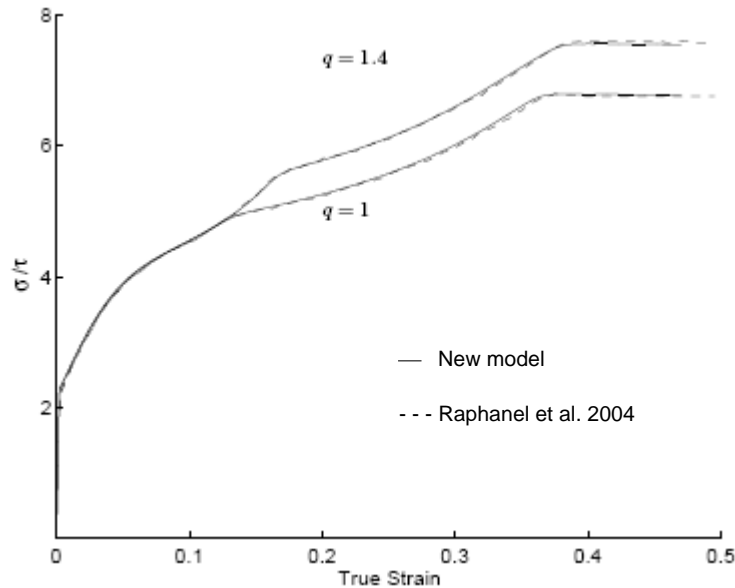


Figure 3: Stress strain curves for uniaxial loading in $[-123]$ direction for $q=1$, and $q=1.4$.

The strain on the slip systems $(111) [-101]$ and $(-1-11) [011]$ versus the global strain of the crystallite and the rotation of the loading axis in the form an inverse pole figure are presented in Figure 4. For the case of $q = 1$, slip is activated on the primary system $(111) [-101]$ and the stress-strain response is stable until a global strain of 15%. At this level of deformation, slip on the secondary or conjugate system $(-1-11) [011]$ is activated, and the loading axis is at the boundary of the primary triangle along the tie line $[001]-[-111]$ in Figure 4b. The rate of accumulation of slip on the former system decreases as can be seen in the plot of slip strains in Figure 4a. This rate is also lower when compared to the rate of slip on the primary system. With further accumulation of slip, the loading direction tends towards the stable $[-111]$ orientation.

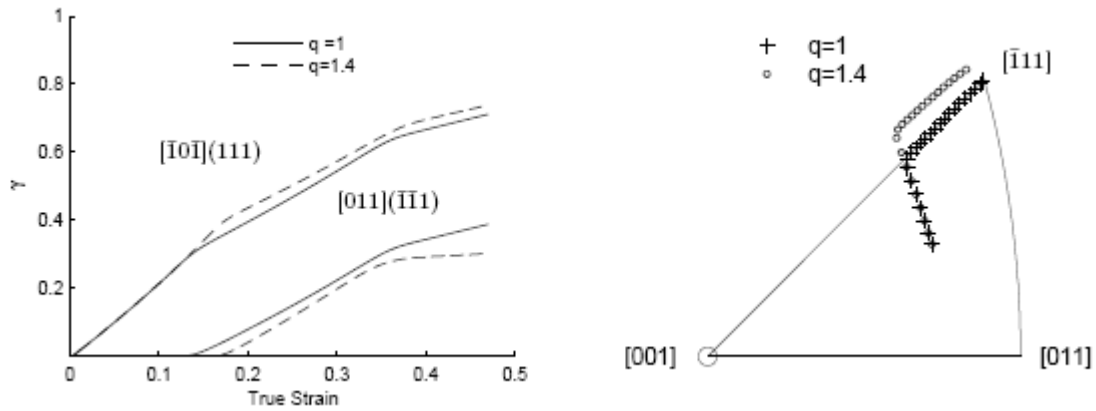


Figure 4: (a) Accumulated plastic slip on active slip systems, (b) Rotation of slip planes showing latent hardening overshoot for $q = 1.4$.

In the case of latent hardening, $q = 1.4$, the stress-strain curve is markedly different. Slip on the primary system is activated as before, but the activation of slip on the secondary system is delayed as a consequence of latent hardening. This causes the loading direction to overshoot the tie line (a discussion of the latent hardening overshoot phenomenon was presented by Anand and Kothari [1996] and is not discussed here). At this level of deformation, slip on the secondary system is activated and the orientation of loading direction is roughly parallel to the tie line, tending toward the stable orientation. For both $q = 1$ and $q = 1.4$, the stress-strain curves from our forward Euler scheme are in excellent agreement with those of Raphanel et al. [2004]. For the plots shown in Figure 4a, in the interest of clarity, we do not show curves from the above reference, but the agreement is, again excellent.

The stress-strain curves for single element computations of simple shearing along $[1-11]$ initially aligned with the X_1 axis and with the X_2 as the normal to the shearing direction are shown in Figure 5. Here, rotation of the slip systems is the main result and comparison of our results with those of Raphanel et al. [2004] show excellent agreement.

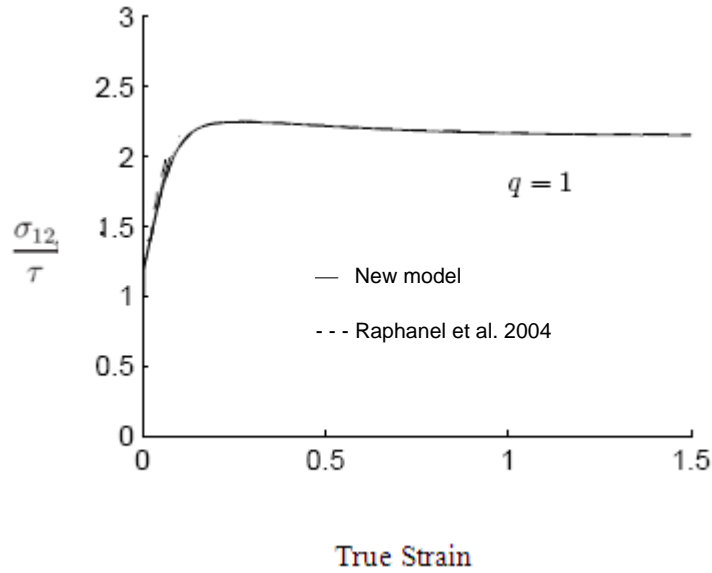


Figure 5: Stress Strain of Single Element Simple Shear

4.1.4 Comparisons of CPU Times: The Rate Tangent versus the Forward Euler Methods

Numerical simulations with identical input files for both the rate tangent method and the forward Euler method were performed. In these simulations, unit cubes were modeled with 8, 27, 64, 125 and 216 elements. The run times for these simulations are presented in Table 2. As expected, an increase in the number of elements corresponded to nearly linear increases in run times with both models (Figure 6). However, the slope of the run time/number of elements curve is much steeper for the rate tangent scheme compared to the forward Euler scheme. This indicates that the efficiency of the new Euler scheme compared to the rate tangent scheme increases with increasing number of elements. This is an expected result since the new model avoids time consuming mathematical operations such as matrix inversions and/or iteration loops which become troublesome with increasing element numbers.

Table 2: Run Times for Both Rate Tangent and Forward Euler Schemes.

Number of Elements	Rate Tangent Run Time (sec)	Forward Euler Run Time (sec)
8	21.399	19.268
27	63.652	42.938
64	171.541	85.128
125	383.925	179.700
216	756.215	331.250

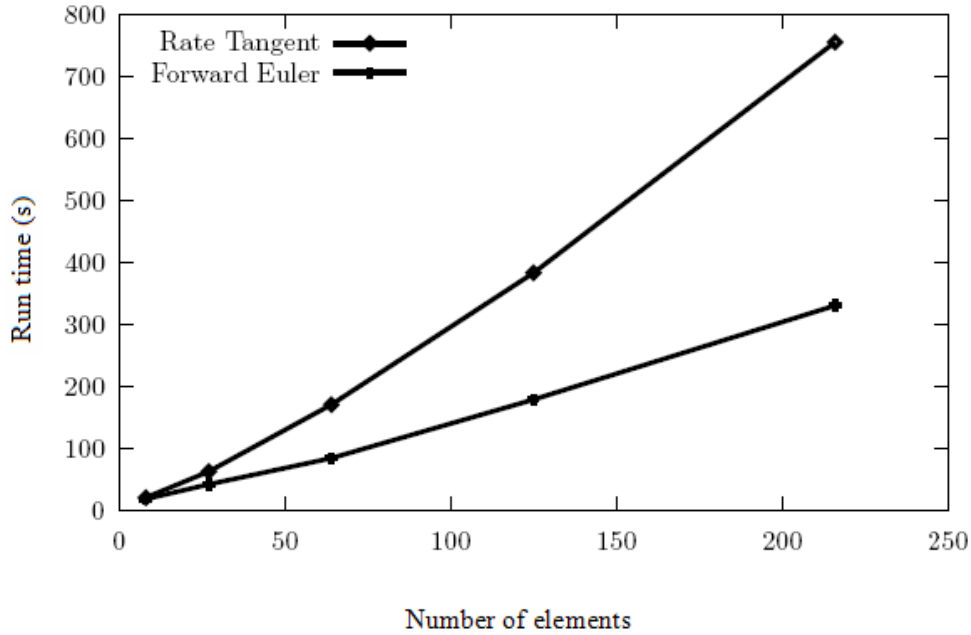


Figure 6: Run Time vs Number of Elements

4.2 Construction of Finite Element Model

The microstructure considered for the first application is representative of wrought 5xxx sheets that consist of FCC aluminum grains and hard intermetallic particles. The three dimensional (3D) polycrystalline microstructure of the aluminum alloy AA5754 is modeled for the second application. The first step in building a model is developing the methods that will produce the sample microstructure and create a complete mesh with texture and particles (if particles are present). Current three-dimensional (3D) data regarding grain structure and orientation can be obtained in voxelized form through serial sectioning as in Schaffer et al. [2007]. A statistically equivalent data set of the voxelized grain data has been created for each application and is explained in Section 4.2.1. Particle data has been obtained from the GM Bangalore lab and is in the form of representative ellipsoids with the locations, dimensions, and orientations of the ellipsoid axes obtained as explain in Tewari et al. [2009]. 3D meshes have been created for each application and is explained in Section 4.2.2.

4.2.1 Construction of Microstructure

The microstructure is generated by using experimental observations from 2 dimensional electron backscatter diffraction (EBSD) maps. Both the grain size-shape distribution as well as the crystallographic orientation (texture) is obtained from EBSD maps. Using the grain geometry and texture data as inputs, a 3 dimensional microstructure is generated. The microstructure is built using a microstructure builder (Brahme et al. [2007]) by the following two steps;

(i) Geometry generation based on experimental observations: The basic assumption in generating a microstructure, which is statistically similar to the observed experimental microstructure, is that all the grains can be approximated as ellipsoids. An ellipsoid is completely described by its semiaxes (a, b, c). From the EBSD maps one can extract the distribution of these a, b and c's. This distribution forms the input to the microstructure builder. Using these, the space is then populated with a set of ellipsoids belonging to the above distribution. The number of ellipsoids generated is far greater than the target number of grains in the microstructure (by about a factor of 2 to 5). Out of these ellipsoids a subset having minimum overlap and filling maximum space is retained.

The next step is to sample the space with randomly distributed points. Each of the points is assigned to one and only one ellipsoid (to which it belongs)¹. Using this set of points as input, Voronoi tessellation is done. The resultant Voronoi cells are assigned to ellipses which contain the original points. Thus we generate a grain structure which is space filling and has no overlap. The resultant microstructure is then sampled on a regular grid to get the voxelized microstructure.

(ii) Adding Texture to the generated microstructure: The EBSD maps are used to calculate the orientation distribution function (ODF) as well as a misorientation distribution function (MDF). The ODF describes the volume fraction of each orientation in the experimental microstructure. The MDF describes the short range ordering of the texture.

The first step of adding texture to the geometry generated in the previous step is to bin both the ODF and MDF data. The next step is to start with a random assignment of texture to the grains. Each grain is assumed to have uniform texture i.e. there is no variation of orientation within the grain. The resultant ODF and MDF of this assignment is calculated. The algorithm proceeds to either swap two orientations or replace the orientation of a grain in the microstructure to minimize the error between the target, experimentally measured ODF and MDF and the calculated ODF and MDF.

¹ If a point is enclosed in more than one ellipsoids it is assigned to the ellipsoid whose centre it is closer too.

Figure 7 shows the resultant microstructure generated using the above procedure for the first application. The microstructure has 50 grains and is sampled on a grid of 10X10X10 voxels in each direction. The grain colors are assigned at random and do not reflect the grain orientations. The assigned texture corresponding to the microstructure is shown in Figure 8.

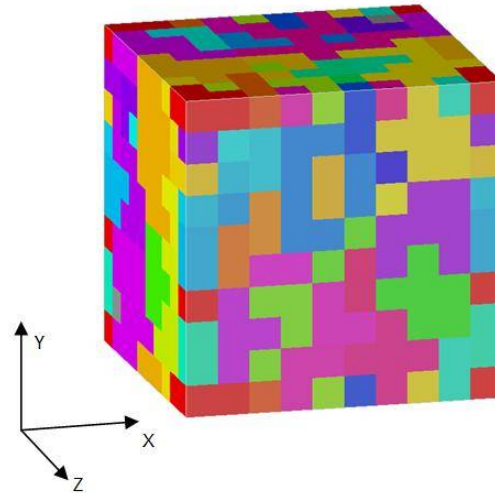


Figure 7: Showing the microstructure generated for the first application using the procedure described in section 4.2.1

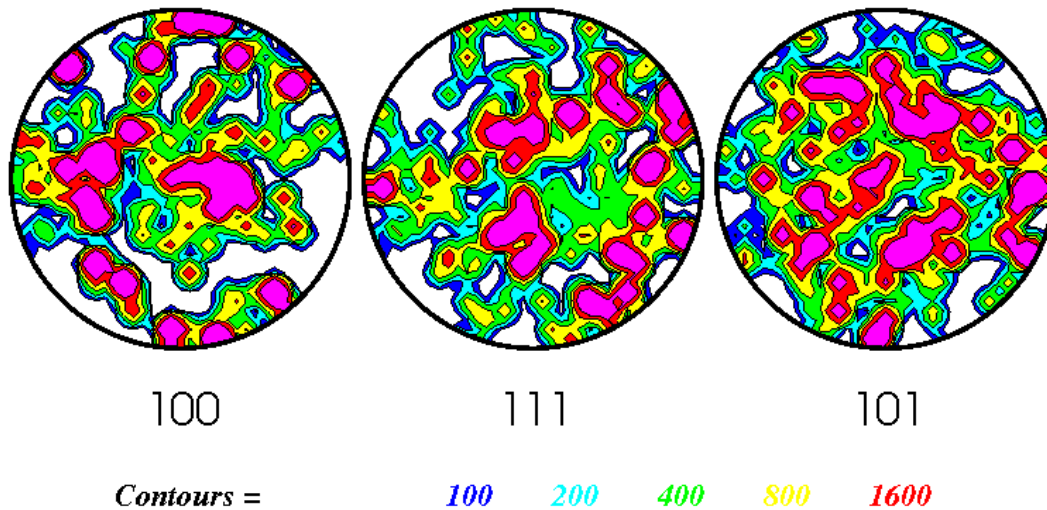


Figure 8: Pole figure showing the fitted texture for the first application using the procedure outlined in section 4.2.1

Figure 9 shows the resultant microstructure generated using the above procedure for the second application. The microstructure has 275 grains and is sampled on a grid of

123X28X3 voxels in X, Y and Z directions respectively. The generated microstructure is three layered. Top and bottom layer are similar because of the periodic boundary conditions. The center layer varies from the outer layers. Figure 10 shows the center layer. The grain colors represent the crystallographic orientation according to the SST color triangle (also shown in the figure). The assigned texture to the microstructure is shown in Figure 11a and the created microstructure is shown in Figure 11b.

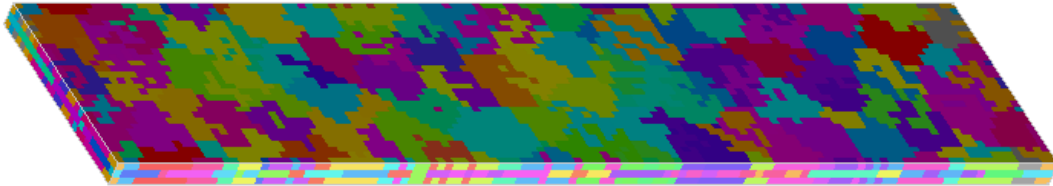


Figure 9: Showing the microstructure generated for the second application using the procedure described in section 4.2.1 (top layer).

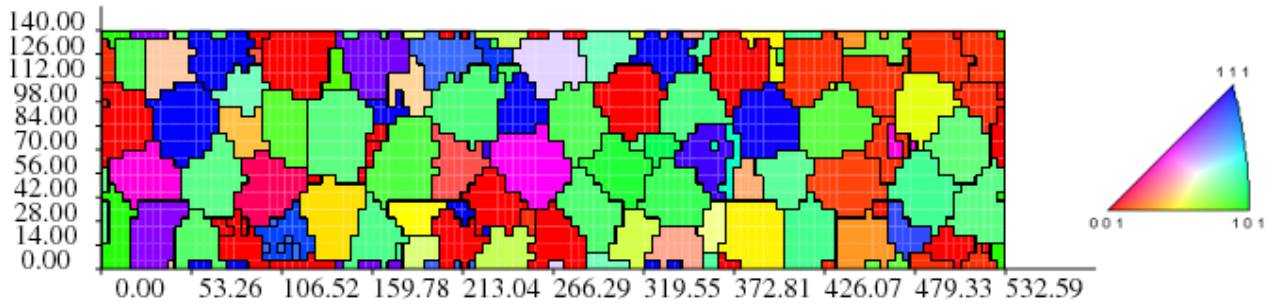


Figure 10: Showing the microstructure generated for the second application using the procedure described in section 4.2.1 (center layer, dimensions in μm).

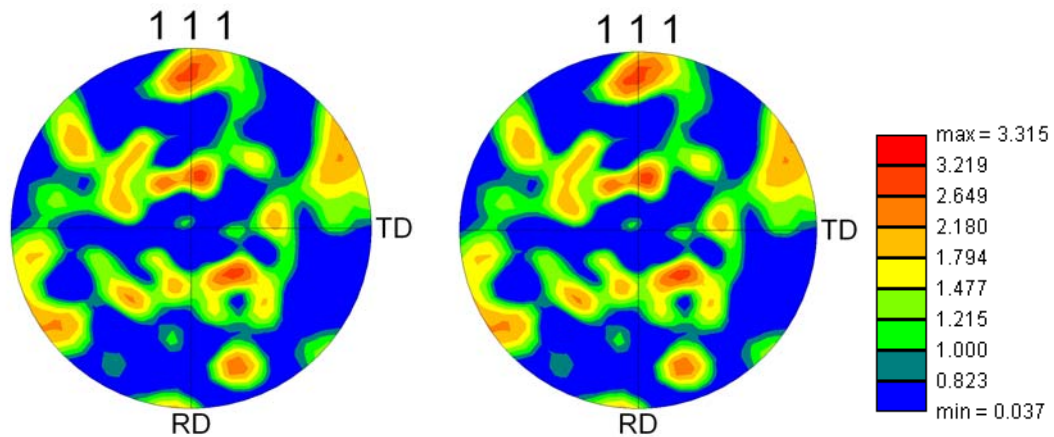


Figure 11: Initial pole figure (a) employed in the procedure outlined in section 4.2.1 and created (b) microstructure used in the second application

In using bulk texture data, one loses information about nearest neighbours interactions. During the reconstruction of the 3D microstructure, matching of ODF and MDF ensures that we capture the nearest neighbouring grain orientations.

4.2.2 Construction of Mesh

Since the texture data is in voxelized form, the generated mesh consists of a 3 dimensional grid of prismatic rectangles with the same dimensions as the texture data resolution. Each rectangle consists of a whole number of hexahedral elements. First the texture data is read to record the number of voxels along each of the axes and their dimensions. A grid of nodes is created that represents the corners of each element with the assigned node number uniquely identifying the node's relative location within the grid. The texture data is then read again to build the list of nodes surrounding the elements within a voxel, and to establish whether or not each element is a part of a particle or grain. Differentiating between a particle or grain element is done by comparing the corner of the element closest to the origin with a set of equations derived for each particle. The element connectivity is generated with a separate part number for grain element versus particle element. The texture file is also created during this pass; it matches the element numbers of each voxel with the euler angles of that voxel. Since the elements within particles do not need texture information, the euler angles for these elements are ignored.

The set of equations in the second pass that establish whether or not the element lies within a particle were created as follows. A local to global transformation matrix is formed which transforms a unit sphere located at the origin into an ellipsoid based on any given axis dimensions a , b , c . Then the ellipsoid is rotated to the same orientation as a given particle using the angles available in the particle data. Then the ellipsoid is translated to the location of the given particle. The equations obtained from the local to global transformations are then inverted to get the global to local transformation. By transforming the location of each element to the local coordinate system of each particle, and checking to see if the element lies within the volume of a unit sphere, the element can be identified as a particle element, or grain element. By assigning a different material model to the two different part numbers, the effects of having an embedded particle in a matrix can be simulated. A rigid material model is chosen to represent the particles while the single crystal constitutive model described in Section 3 is used for the matrix. A model can be created without particles by passing an empty particle data file to the executable.

The inherent properties of a mesh formulated in this way include a “welded” interface between the particles and the matrix as well as between grains. Elements on either side of the interface share the same nodes and therefore are incapable of separating or sliding. A

consequence of this mesh is a “staircase” boundary between the particle and the matrix and at the grain interfaces. Since the elements are prismatic rectangles, it is impossible to have a smooth contour along any interface. The jagged shape of the particle to matrix interface can cause stress concentrations, however, since the matrix elements located at the interface are “welded” to rigid elements, the strain in those elements are low. In other words, there is a stress concentration, but it is in a low activity area. This has been confirmed during the simulations. Since we do not have grain boundary sliding due to the welded elements, we do not need to worry about the rough interface’s influence on interface slip.

5. Applications

In the first application, we employ the numerical model described above to simulate two- phase microstructures for FCC materials. This work has been submitted as a paper to the International Journal of Plasticity, (Rossiter et al. [2009b]).

In the second application, we investigate the effects of strain paths, strain rates and thermal softening on the formation of localized deformation. This work has been submitted as a paper to the International Journal of Plasticity, (Rossiter et al. [2009a]).

5.1 Two-Phase Microstructures

A 10 μm cube sample microstructure with a 1 μm resolution was created as outlined in Section 4.2.1. The microstructure contained 51 grains and is shown in Figure 7. The mesh was created with 3 particles located in positions shown in Figure 12. Since the particles average 3 μm 's in length, each voxel was sub divided into 5 elements along each axis (125 elements). This allowed the elements to more accurately represent the particle surface. Three simulations were performed, one with no particles, one with the three particles as seen in Figure 12, and a final simulation with the large particle shifted into a high strain region of the second simulation (Figure 13). The mesh for the second simulation can be seen if Figure 14. The overall unit convention for the simulations can be seen in Table 3. The boundary conditions and loading for the simulations are as follows. The $x=0$ axis, the $y=0$ axis and the $y=10 \mu\text{m}$ are constrained, while the $x=10 \mu\text{m}$ axis is pulled at a constant velocity (Figure 7). The imposed boundary conditions simulate in-plane plane strain which is the common deformation mode for failure during metal forming operations.

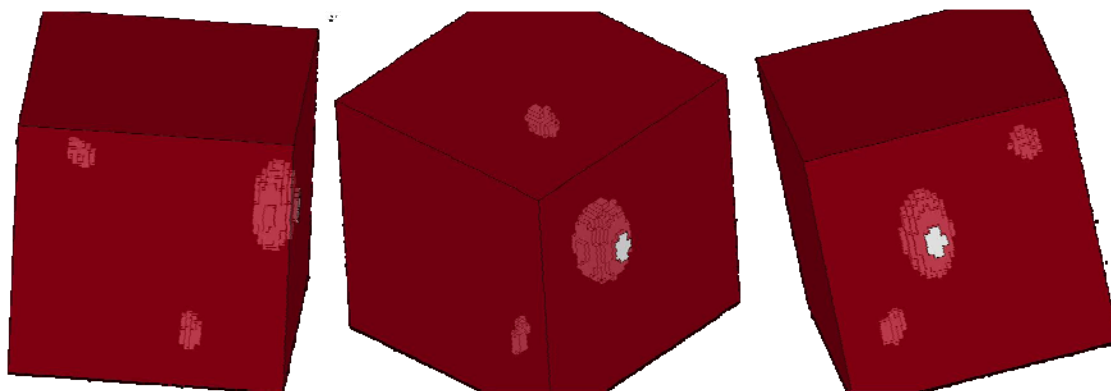


Figure 12: Particle Locations for Second Simulation

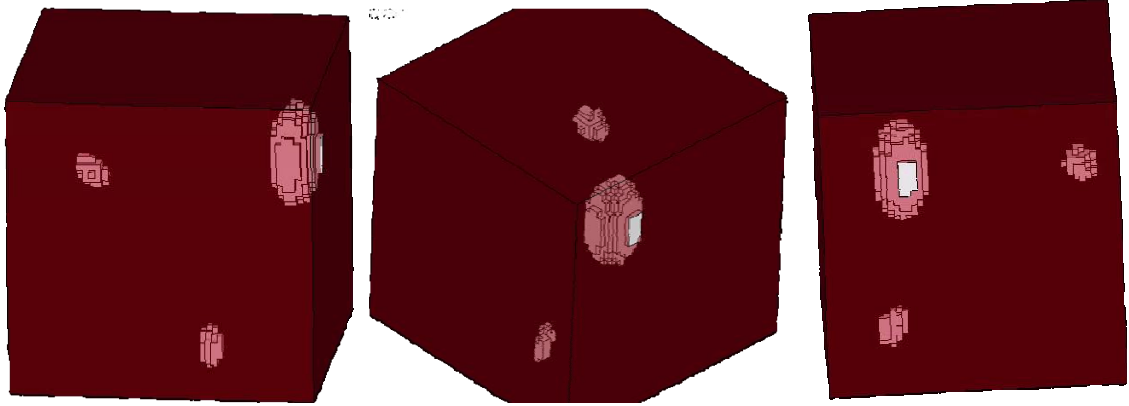


Figure 13: Particle Locations for Third Simulation

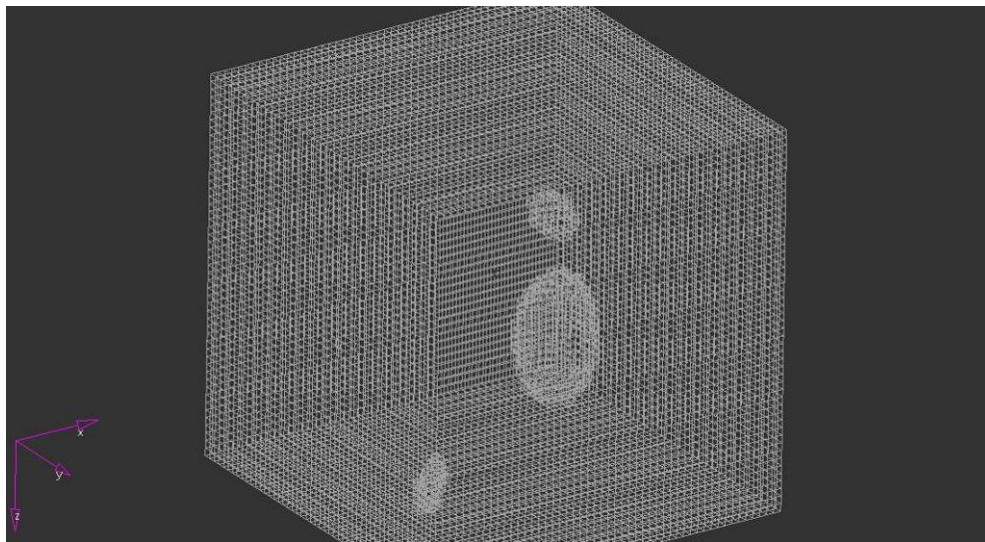


Figure 14: Mesh for Second Simulation

Table 3: Unit Convention.

Measurement	Time	Length	Mass	Force	Stress
Unit	μs	μm	ng	μN	MPa

5.1.1 Results and Discussions

The results presented in this section are contour plots of maximum principal strain obtained after a macroscopic strain of 7%. While the overall strain is small, it can be seen that heterogeneous deformation has clearly formed as represented by elements with strain more than 28%. Figure 15 presents the contour plots of maximum principle strain for the first simulation (no particles). It can be seen that there is a diagonal plane of high strain, roughly 45° from the plane of loading, which most likely is a shear band in the material. Figure 16

shows the maximum principal strain for the second run with the same texture as first run, but with some of the grain elements replaced by particle elements. The model excludes particle de-cohesion with the matrix and particle fracture. The same shear band can be seen, while, the elements within a parallel band that crosses through the particle are all of lower strain, and the elements within a parallel band that lies next to the particle is of higher strain. It appears as if the particle acts as a barrier for the shear band. The strain that was originally located along the band where the particle now resides appears to have been shifted up and concentrated the strain in the rest of the original band. For the final simulation, the particle that resided on the edge of the original (no particles) band was shifted so that it now lies directly in the original band. The principal strain results for this third run can be seen in Figure 17. The band is almost completely absent. The particle seems to have inhibited the band from forming in the simulations. Inal et al. [2008] also reported a change in location of localization when particles are added to texture.

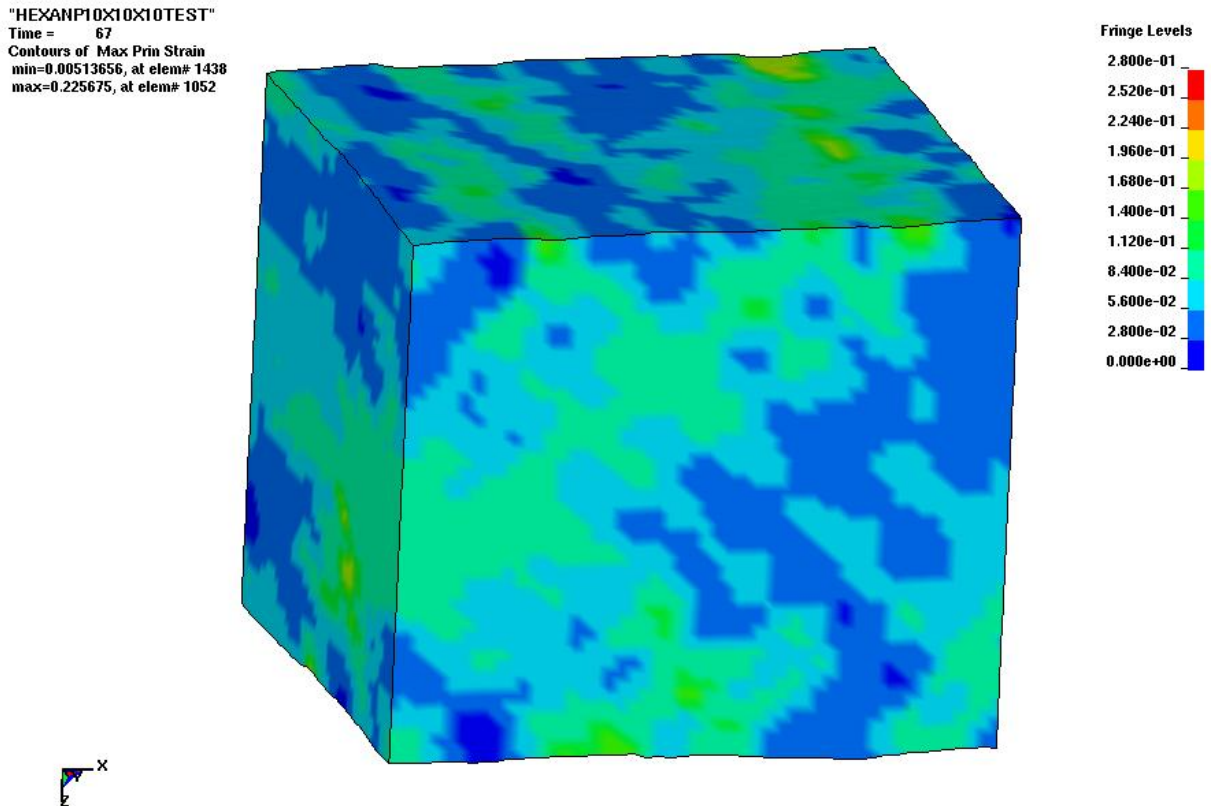


Figure 15: Maximum Principle Strain with No Particles (First Simulation).

Time = 67
Contours of Max Prin Strain
min=0, at elem# 35475
max=0.874029, at elem# 64967

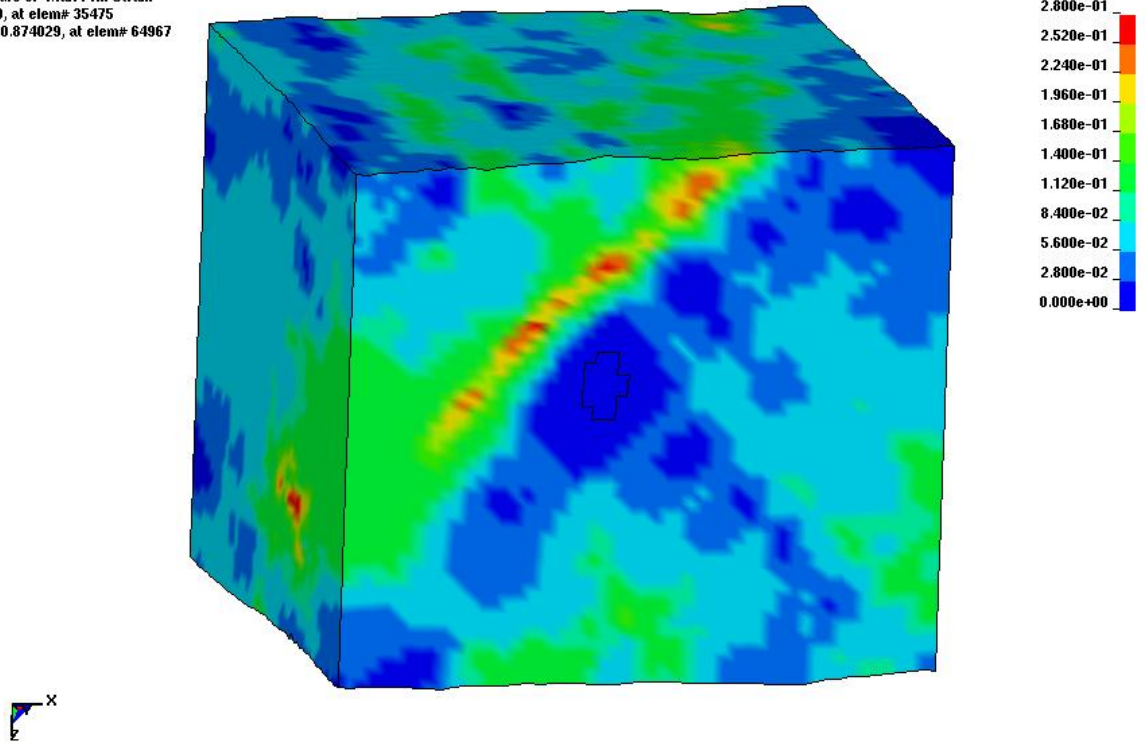


Figure 16: Maximum Principle Strain with Particles (Second Simulation).

Time = 67
Contours of Max Prin Strain
min=0, at elem# 10300
max=1.00326, at elem# 64967

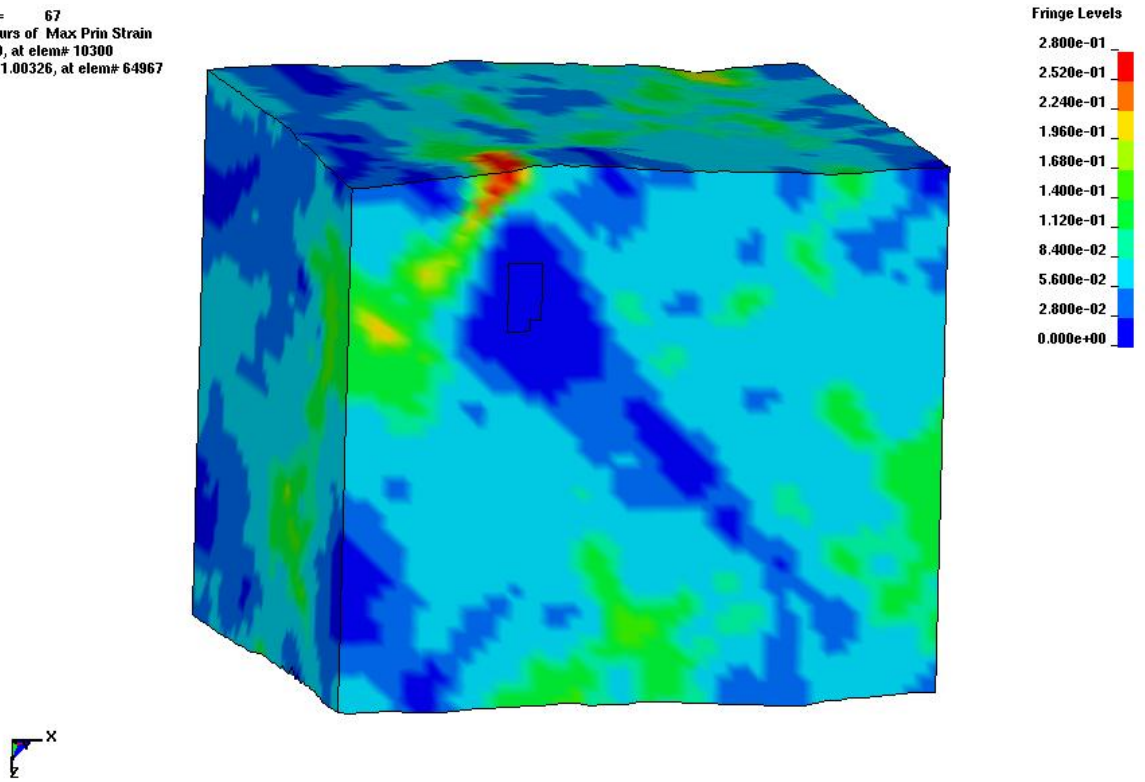


Figure 17: Maximum Principle Strain with Moved Particle (Third Simulation).

We next present contour plots of maximum principle strain from sections cut at various depths from the front face (Figure 18). Figure 18 and Figure 19 present contour plots for sections cut at $4\ \mu\text{m}$ and $3\ \mu\text{m}$ from the front face respectively. Note that, for the second and third set of simulations, only the large particle was moved; the two small particles were kept at constant positions. Our simulations clearly indicate that, changing the place of a particle not only affects the strain distribution in the very close vicinity but also affects the strain distribution throughout the three dimensional material.

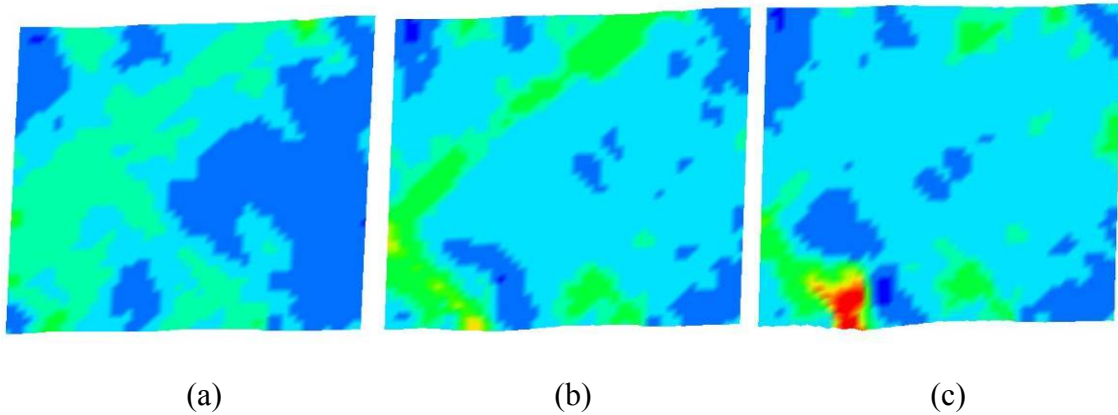


Figure 18: Max. Prin. Strain For (a) No Particles, (b) Particles, and (c) Moved Particle ($4\ \mu\text{m}$ in).

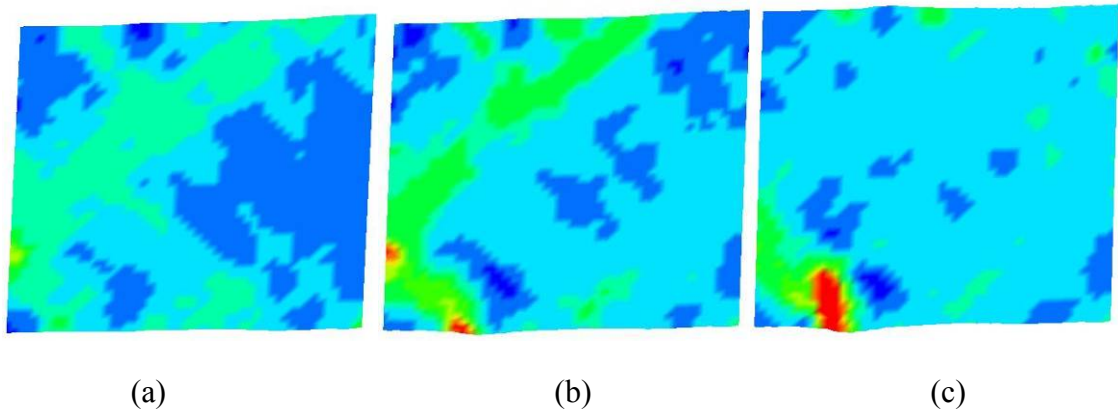


Figure 19: Max. Prin. Strain For (a) No Particles, (b) Particles, and (c) Moved Particle ($3\ \mu\text{m}$ in).

Finally, we compare the stress concentrations in the above three runs (in the form of the highest value regardless of its location). Incorporating particles in the matrix increases the

maximum predicted stress by 380% compared to the run without particles. Furthermore, simulations show that the particle locations are important; there is a difference of 15% in the predicted maximum stress between the second and the third runs.

5.2 Shear loading of Al5754

A 532.6 μm x 140 μm x 13 μm (x,y,z-dimensions) sample microstructure with approximately a 4.5 μm resolution was created as outlined in Section 4.2.1. The microstructure contained 275 grains and the center layer can be seen in Figure 10. The material properties used in the simulation can be seen in Table 4. Three items were varied during the simulations: strain path, strain rate, and whether or not thermal softening was included. Three different strain paths were tested: simple shear up to 60%, 12% tension followed by 60% simple shear, and 12% tension with 60% simple shear applied simultaneously. Three different strain rates were chosen: 300/s, 1000/s and 3000/s. 300/s is in the range of strain rates seen in an automotive crash, while the remaining strain rates were chosen to observe the strain rate effects (Bleck et al. [2004]). In order to observe the effect of thermal softening on the simulations, two cases were set up for each simulation: no thermal softening, and 100% of plastic work converted to thermal softening. A total of 18 separate simulations were completed for this study. The simulations use the explicit version of LS-Dyna. No time scaling or mass scaling was used. The overall unit convention for the simulation is listed in Table 3.

Table 4: Material Properties

Property	$\dot{\gamma}$	h_0	m	τ_0	n
Value	0.001 1/s	6900 MPa	0.02	23 MPa	0.21
Property	q	ρ	C_p	T_{ini}	T_{melt}
Value	1	2.64 g/cm ³	900 J/Kg·K	300 K	934 K

The boundary conditions and loading for the simulations are as follows. The $z=0$ plane is constrained in the z -direction to prevent buckling of the model. All the nodes on the $x=0$ plane are paired with their respective node on the opposite surface, and zero relative displacement is allowed. This enforces a periodic boundary condition and allows elements on either side of the boundary to contribute to the location of the nodes. The $y=0$ plane is constrained in the y -direction and x -direction. Finally, all the nodes on the upper $y=140 \mu\text{m}$ surface are given an imposed displacement dependant on the strain path and strain rate of the simulation.

The thermal softening is achieved by first calculating the plastic work for each element.

$$\mathbf{W} = \boldsymbol{\sigma}_{(n)} \boldsymbol{\varepsilon}_{(n)} \quad (38)$$

The total energy of the element is then updated using a fraction (f) of plastic work converted to energy. In our simulations involving thermal softening, $f = 1$ in order to maximise the temperature rise.

$$\mathbf{E}_{(n+1)} = \mathbf{E}_{(n)} + f\mathbf{W} \quad (39)$$

The new temperature is then calculated using density (ρ) and specific heat (C_p).

$$\mathbf{T}_{(n+1)} = \mathbf{E}_{(n+1)} / (\rho C_p) + \mathbf{T}_{initial} \quad (40)$$

The softened yield strength for each element is then calculated based on the yield strength without thermal softening, and the temperature relative to the melting point.

$$\tau_{ys(n)} = \tau_{y(n)} \left[1 - \frac{(\mathbf{T}_{(n)} - \mathbf{T}_{room})}{(\mathbf{T}_{melt} - \mathbf{T}_{room})} \right] \quad (41)$$

Since no heat transfer is used in this model, the temperature rise is non-reversible and maximised. This would promote more local irregularities than if the effects of temperature rise were more evenly distributed amongst neighbouring elements. It should be noted that dynamic re-crystallization was not considered during these simulations.

5.2.1 Results and Discussion

The results of the simulations, outlined in section 5.2, are reported as contour plots. Figure 20, Figure 21, and Figure 22 show the contour plots of xy shear strain for each strain path at 300/s and with no thermal softening. The distribution of strain changes with the strain paths, the strain path with simultaneous tension and shear shows a higher strain band in the lower section of the sample, while the other two strain paths show an upper and lower band in the sample. The simulation with initial tension, and then shear shows higher strain in the upper band while simple shear shows higher strain in the lower band. As strain rate is increased and thermal softening is added, the strain distributions for the three different strain paths do not change indicating that when texture is constant, strain distribution is only dependant on strain path.

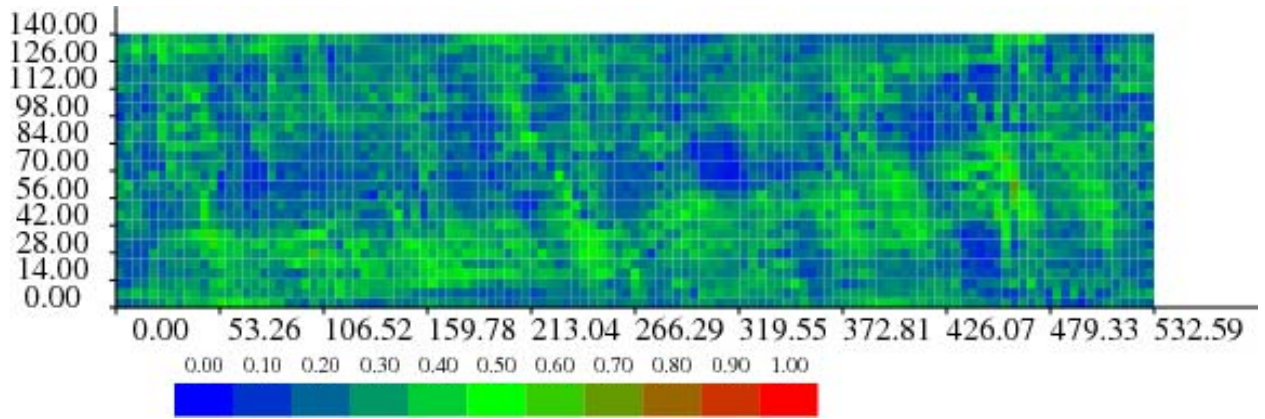


Figure 20: Contour Plot of xy strain at 300/s with No Thermal Softening for Simple Shear.

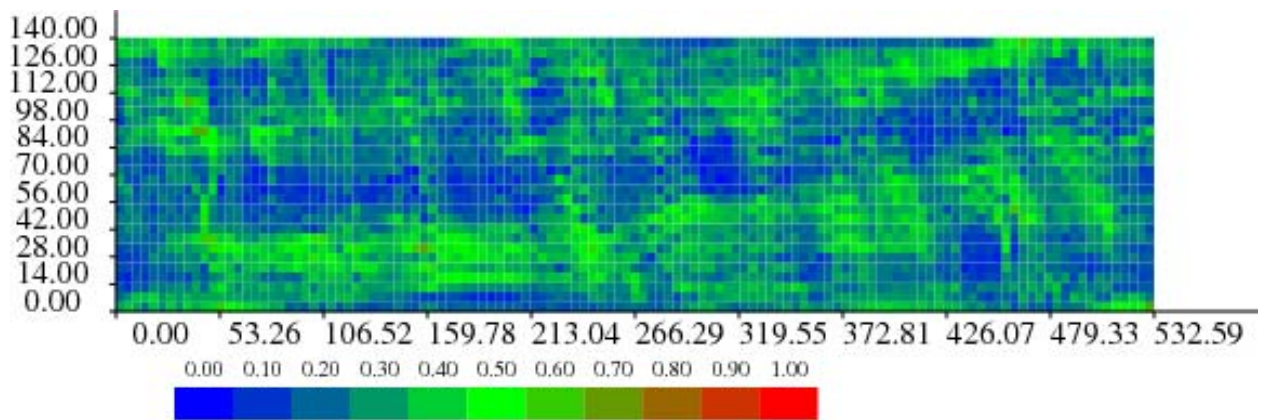


Figure 21: Contour Plot of xy strain at 300/s with No Thermal Softening for Tension Followed by Shear.

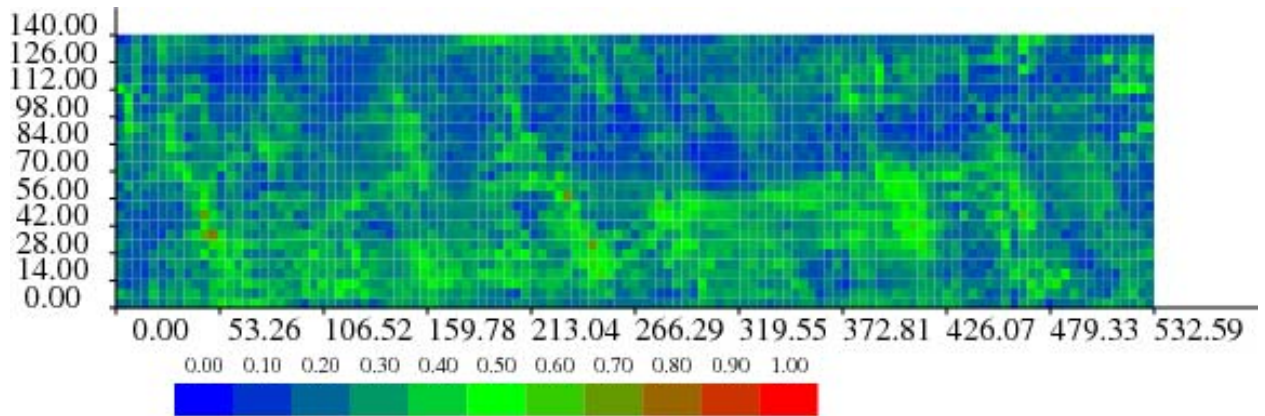


Figure 22: Contour Plot of xy strain at 300/s with No Thermal Softening for Simultaneous Tension and Shear.

The effective stress versus applied shear strain curves for all the simulations are presented in Figure 23, Figure 24, and Figure 25. The curves are grouped by strain path. As expected, the average stress increases as strain rate increases. Thermal softening reduces the averaged stress for each scenario. Thermal softening appears to have more of an effect on the tension followed by shear simulations and the simple shear simulations. The simultaneous tension and shear simulations do show a lower average stress with thermal softening, however the drop is not as pronounced.

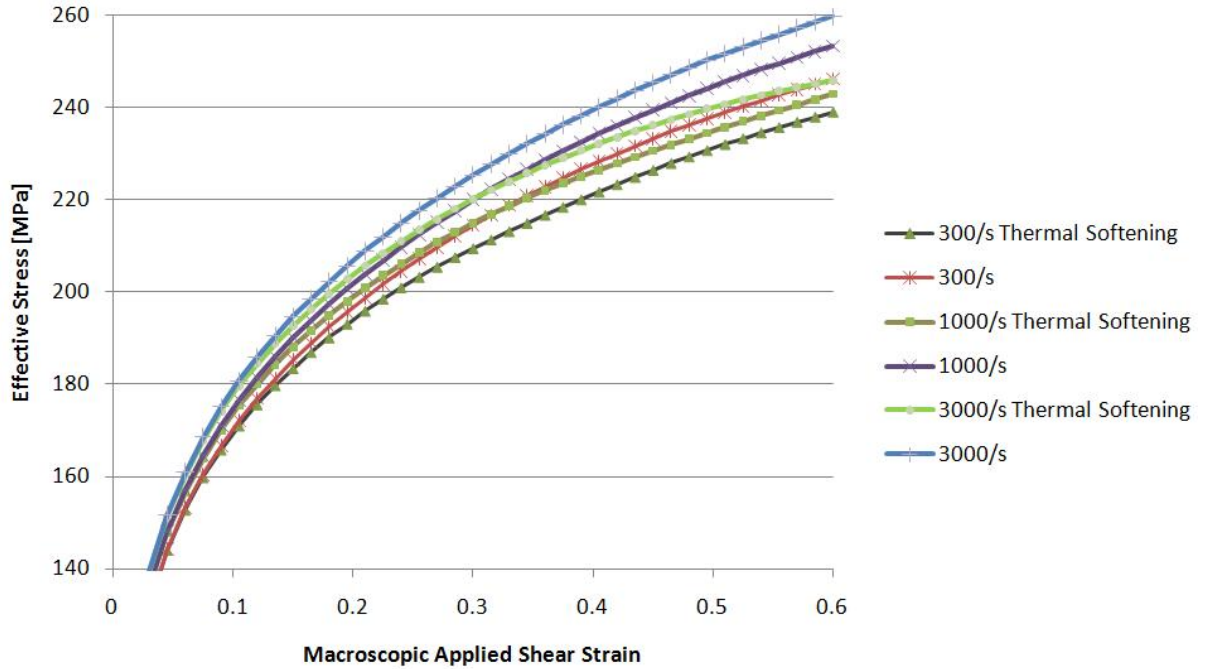


Figure 23: Simple Shear Average Stress Strain Curves.

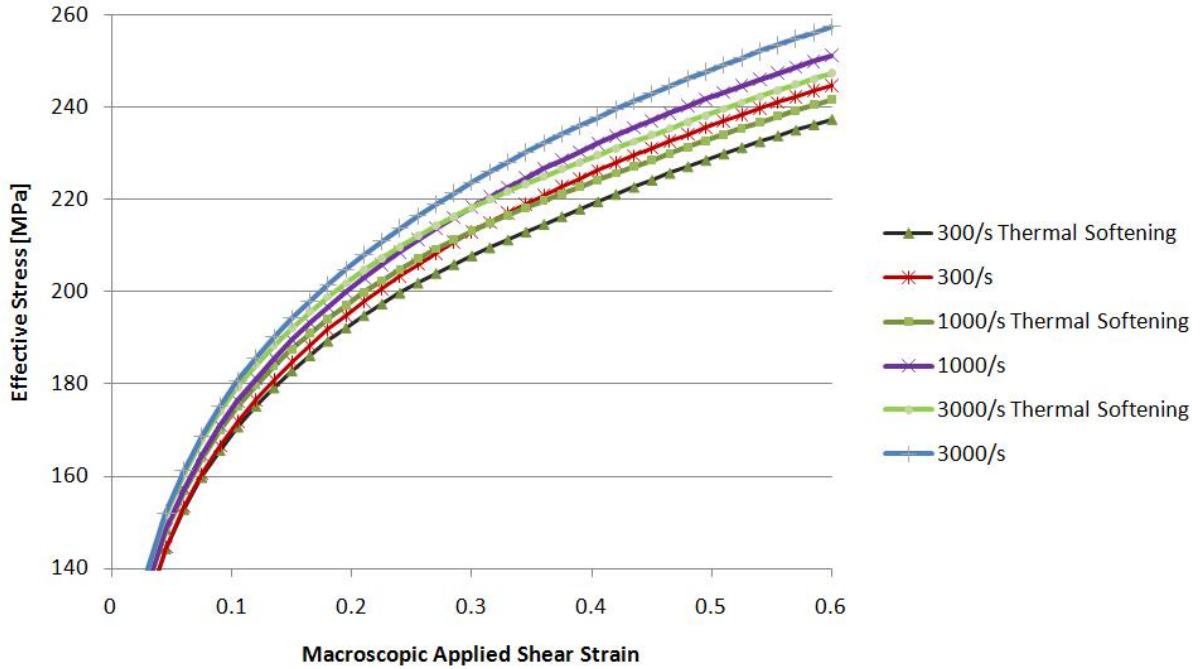


Figure 24: Simultaneous Tension and Shear Average Stress Strain Curves.

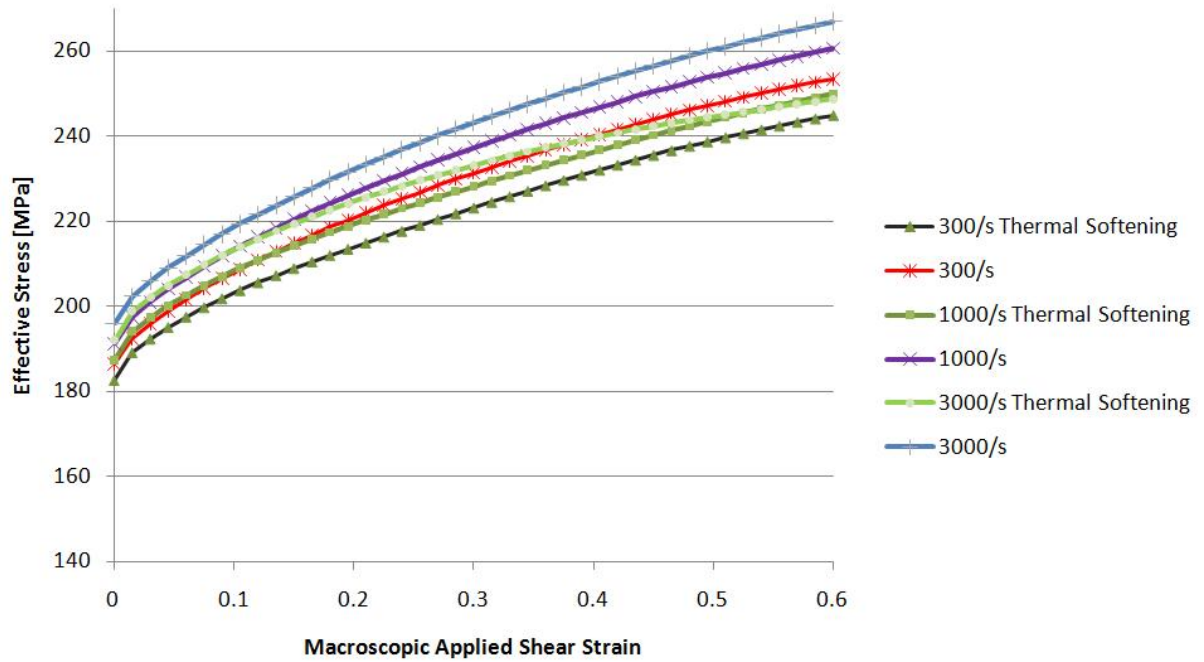


Figure 25: Tension Followed by Shear Average Stress Strain Curves.

The average xy shear strain for the three different strain paths without thermal softening are as follows: pure shear is 0.27, simultaneous tension and shear is 0.267, and tension followed by shear is 0.275. These average strains do not change with strain rate,

however they all drop by 0.001 when thermal softening is added. Table 5 shows the standard deviation of xy strain for all the simulations. It can be seen that as strain rate increases when thermal softening is excluded, the standard deviation decreases indicating that the material acts more homogeneously. However when thermal softening is added, the standard deviation becomes unpredictable. When thermal softening is added, standard deviation consistently increases from the no thermal softening case indicating that thermal softening increases the non-uniformity of xy strain. The isothermal data supports the findings that increased strain rates reduce localization. The adiabatic data indicates that when thermal softening is at its highest (100% plastic work converted to heat and no heat dissipation), the effect of strain rate increase is removed in the simulation.

Table 5: Standard Deviation (SD) of xy strain

Thermal Softening	Strain Path	Average xy Shear Strain	300/s SD	1000/s SD	3000/s SD
No	Shear	0.27	0.09168	0.09135	0.09081
No	Simultaneous	0.267	0.09551	0.09538	0.09494
No	Tension First	0.275	0.10649	0.10572	0.10531
Yes	Shear	0.269	0.09557	0.09652	0.09638
Yes	Simultaneous	0.266	0.10121	0.10259	0.10235
Yes	Tension First	0.274	0.11408	0.11452	0.11680

Figure 26 shows the increase in strain when thermal softening is added versus the strain magnitude without thermal softening for the tension followed by shear at 3000/s simulation. The line of best fit is drawn to act as an aide to see the trend in the data. It can be seen that the areas with higher strain tend to increase in strain when thermal softening is added, however areas with low strain tend to decrease. Figure 27 shows a contour plot of the same strain increase and it can be seen that the bands of high shear in Figure 28 are seen again as bands of strain rise. Every simulation displayed the same trend and the slopes of the trend lines can be seen in Table 6. The slopes consistently rise as strain rate increases indicating a more pronounced difference when thermal softening is added. This supports the conclusion that the addition of thermal softening increases the localization in the simulations and that increasing the strain rate increases that effect.

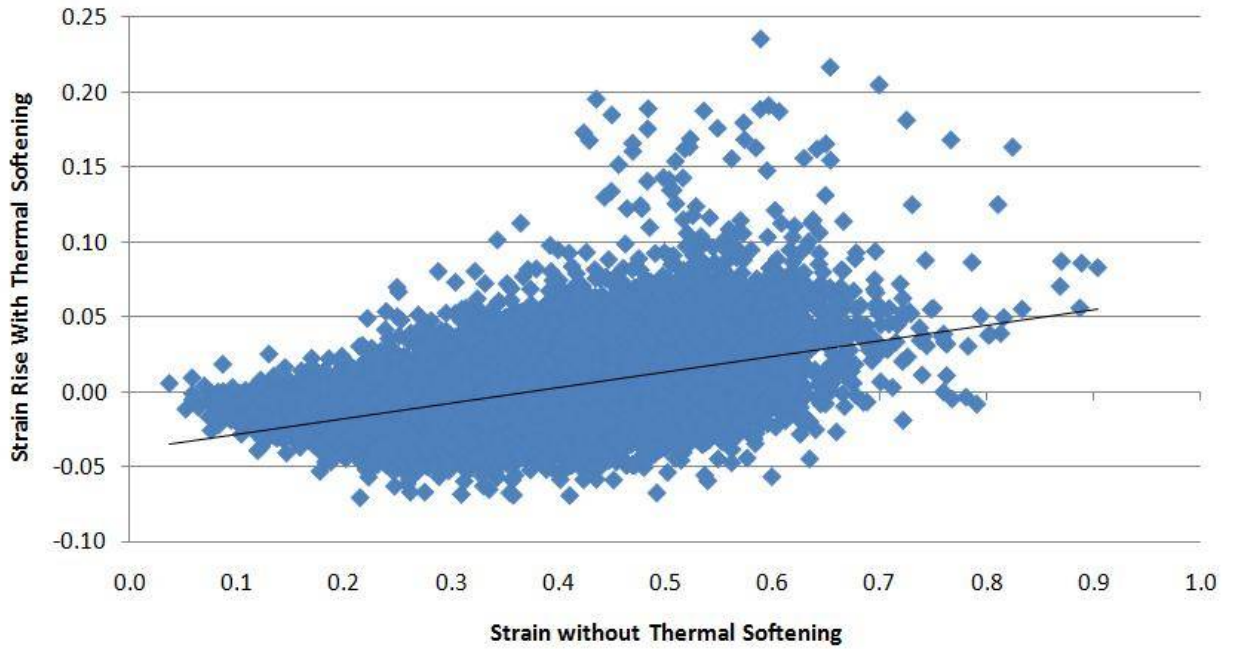


Figure 26: Strain Rise with Thermal Softening vs. Strain without Thermal Softening for Tension Followed by Shear at 3000/s.

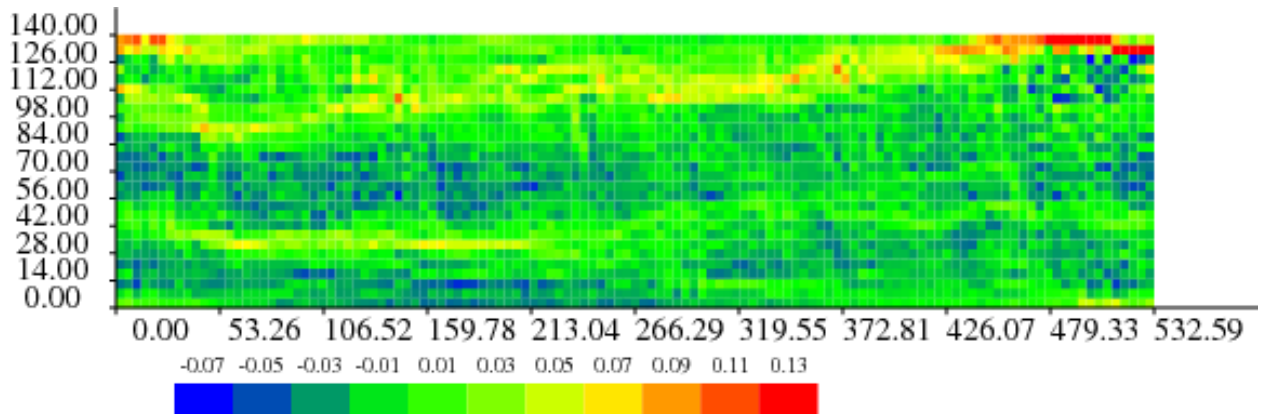


Figure 27: Contour Plot of the Difference in Effective Strain when Thermal Softening is Added to Tension Followed by Shear at 3000/s.

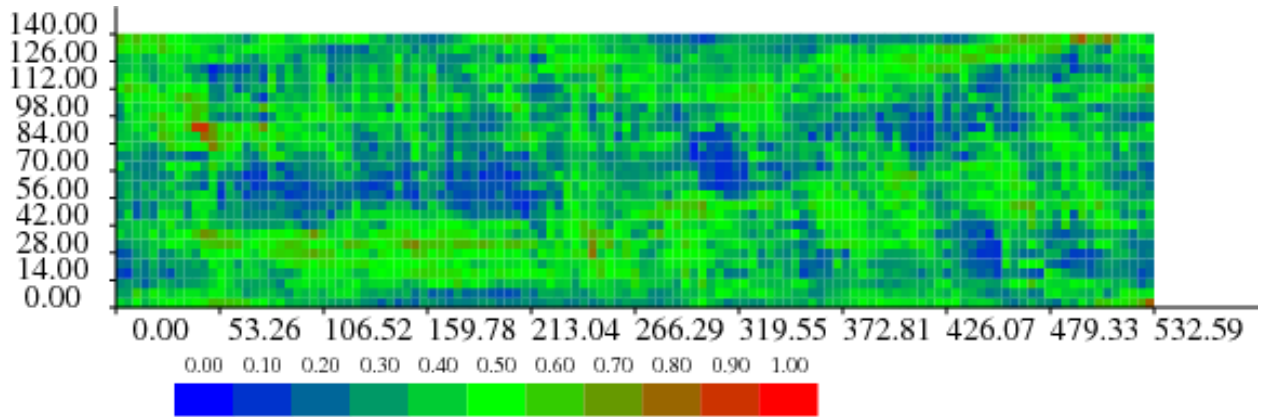


Figure 28: Contour Plot of Effective Strain for Tension Followed by Shear at 3000/s with No Thermal Softening.

Table 6: Slope of Strain Rise vs Strain with Thermal Softening

Strain Path	300/s	1000/s	3000/s
Shear	0.0484	0.0639	0.0696
Simultaneous	0.0705	0.0887	0.0911
Tension First	0.0703	0.0794	0.1044

The difference in strain magnitudes between simulations which exclude thermal softening and their respective simulations which include thermal softening is very small when compared to the difference between the high strain and low strain regions within the simulations excluding thermal softening. Figure 28 and Figure 29 show this trend for tension followed by shear at 3000/s and this trend is seen throughout the simulations. This would indicate that when strain rates are in the range of 300/s to 3000/s, the geometrical softening dominates over the thermal softening when the effects of dynamic re-crystallization are excluded.

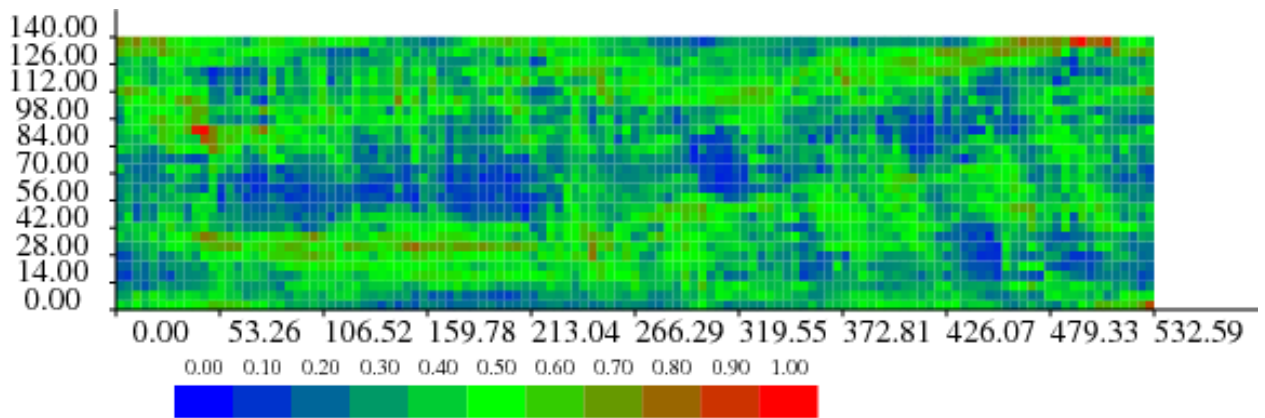


Figure 29: Contour Plot of Effective Strain for Tension Followed by Shear at 3000/s with Thermal Softening.

When observing Figure 30 and Figure 31 we can clearly see a good match between the areas that have rotation and the outlines of the grains for both layers. Since the two layers are quite different from one another, the material along the through thickness does not all contain the same orientation. That would indicate that the rotation of a grain is highly dependant on the initial orientation of that grain regardless of what the neighbouring grains are doing. When observing the xy strain figures for the same loading, Figure 32 and Figure 33, we see that the overall distribution of strain between the two layers are very similar indicating that the strain distribution through the thickness must be compatible regardless of whether one of the orientations does not initially favour strain. Figure 34, Figure 35 and Figure 36 show the onset of effective strain for the Simple Shear strain path at 300/s without thermal softening for $z=0$, $z=6.5$ and $z=13$ layers respectively. The macroscopic strain is at 1.5% and it can be seen that the concentrations are at grain boundaries. Each layer has a unique set of hot spots shown in red indicating that the initial strain on a layer is independent of the other layers. Since the final strains at the end of the simulations were uniform through all the layers, this would indicate that at some point regions of localized strain on one layer spread over the other layers and vice-versa.

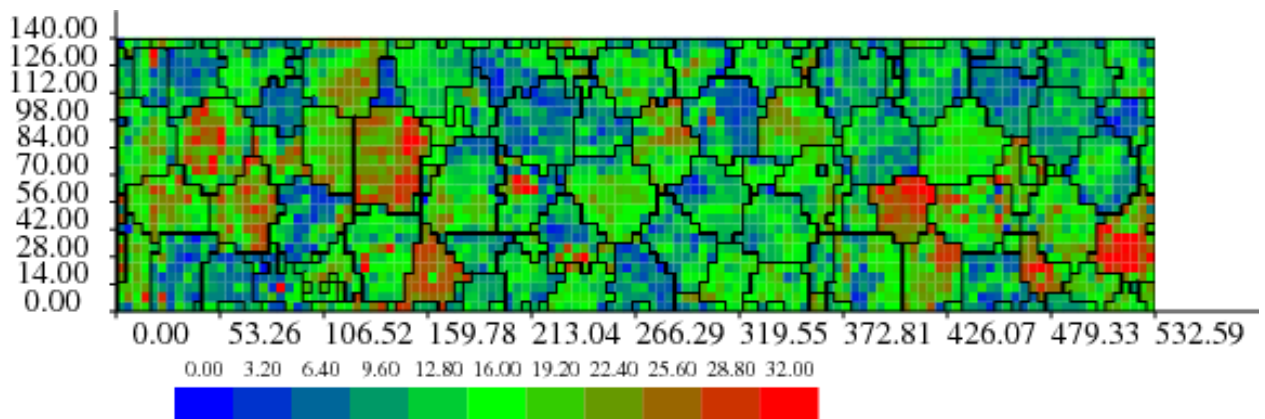


Figure 30: Contour Plot of Misorientation Change for Simultaneous Tension and Shear at 300/s Without Thermal Softening (center layer).

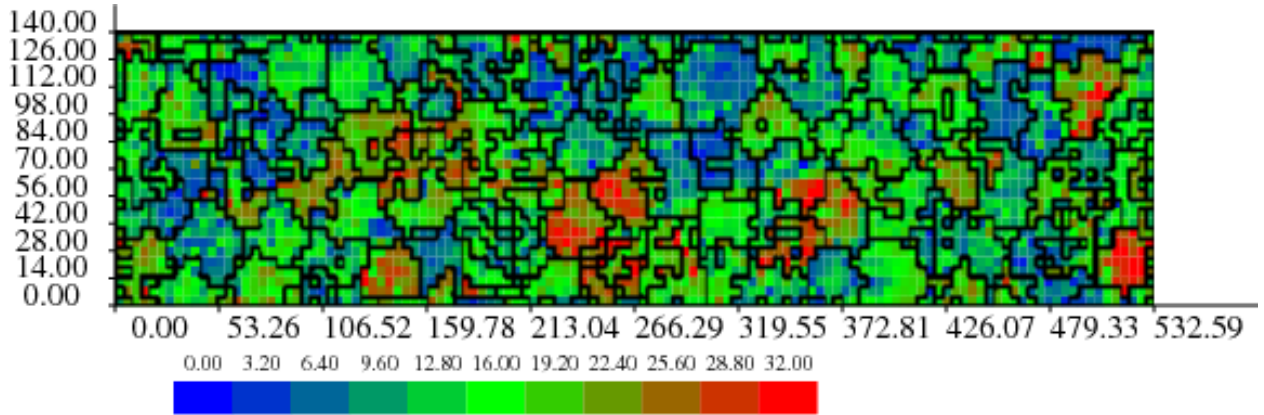


Figure 31: Contour Plot of Misorientation Change for Simultaneous Tension and Shear at 300/s Without Thermal Softening (top layer).

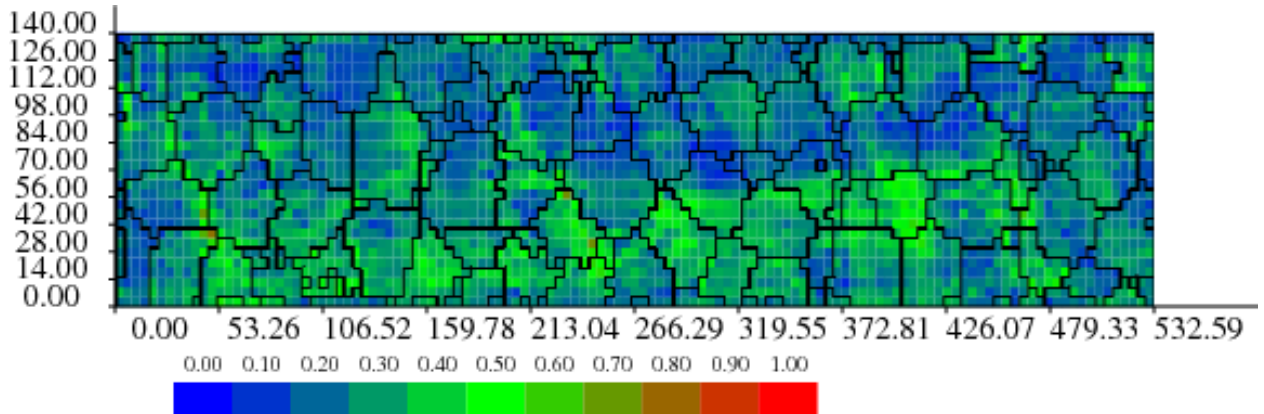


Figure 32: Contour Plot of xy Strain for Simultaneous Tension and Shear at 300/s Without Thermal Softening (center layer).

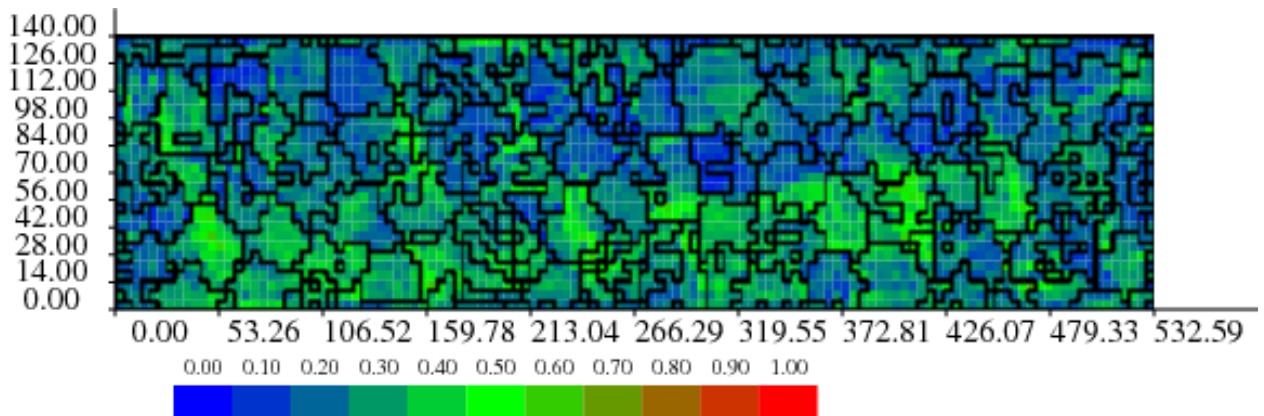


Figure 33: Contour Plot of xy Strain for Simultaneous Tension and Shear at 300/s Without Thermal Softening (top layer).

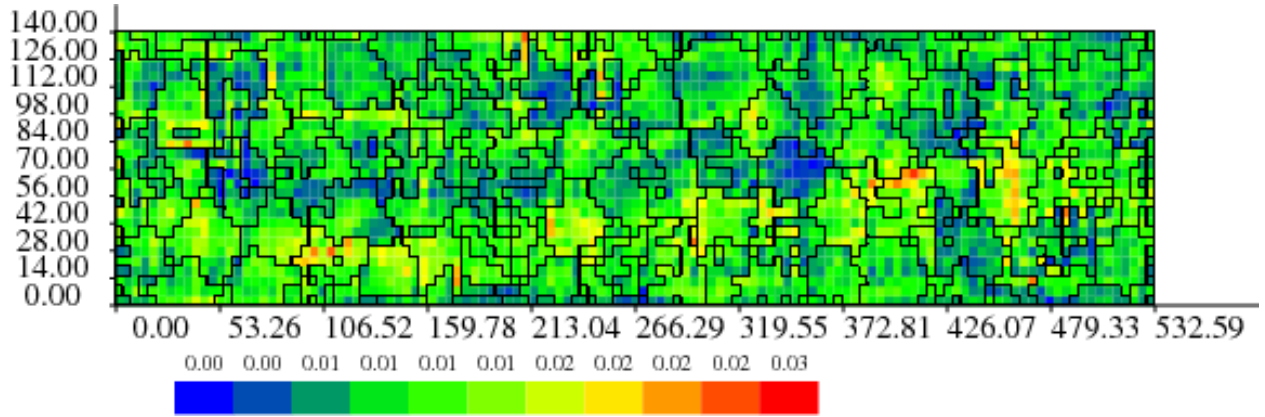


Figure 34: Contour Plot of Effective Strain at 1.5% Simple Shear at 300/s without Thermal Softening (bottom layer).

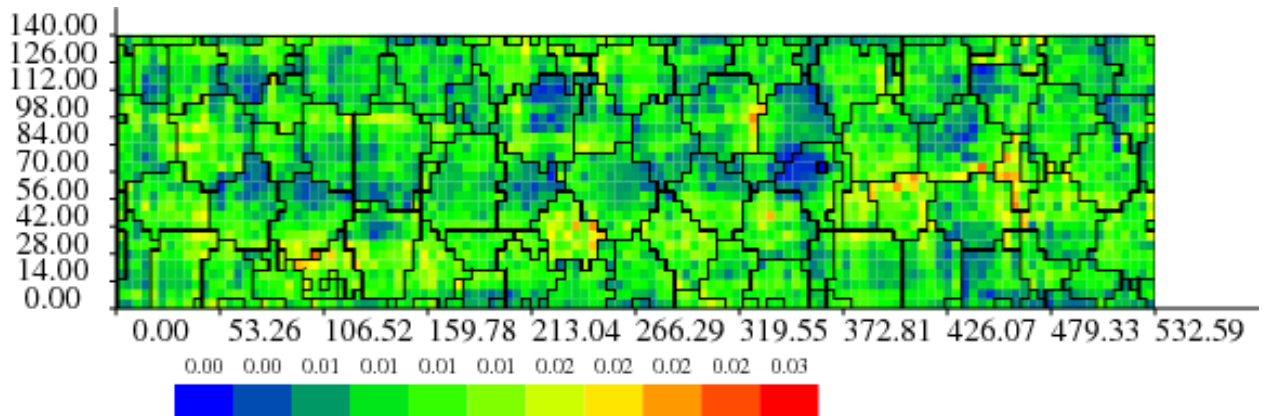


Figure 35: Contour Plot of Effective Strain at 1.5% Simple Shear at 300/s without Thermal Softening (center layer).

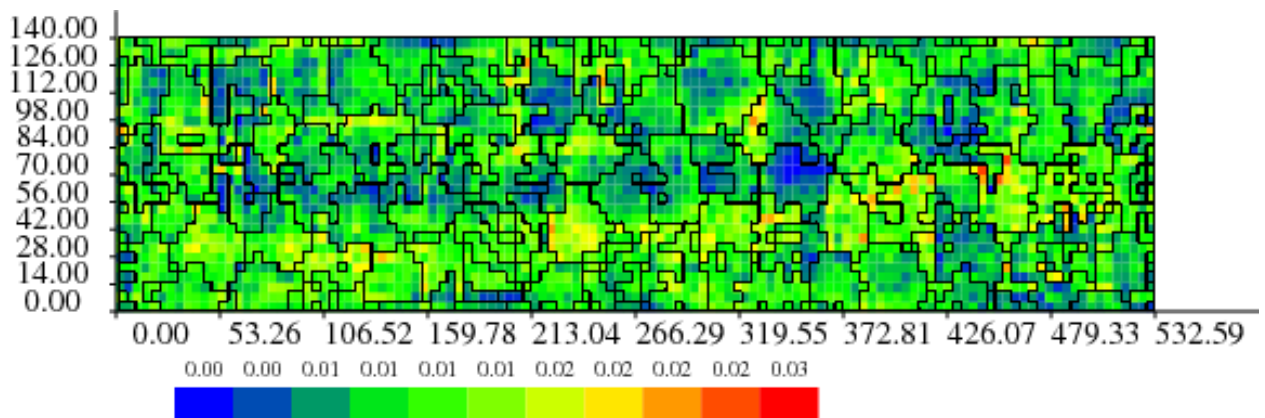


Figure 36: Contour Plot of Effective Strain at 1.5% Simple Shear at 300/s without Thermal Softening (top layer).

The simulated texture evolutions are presented in Figure 37, Figure 38 and Figure 39. It can be seen that, for the strain path of simple shear, the typical shear texture is predicted where increasing the strain rate resulted with slightly sharper textures (Figure 37a-c). Simulations show that while the predicted textures for the strain path of tension followed by shear (Figure 39) is very similar with the textures predicted for simple shear, the textures predicted by the strain path of simultaneous tension and shear differ significantly (Figure 39). Furthermore, for the latter two strain paths, simulations predict that the strain rate has very little effect on the evolved textures (Figure 38 and Figure 39).

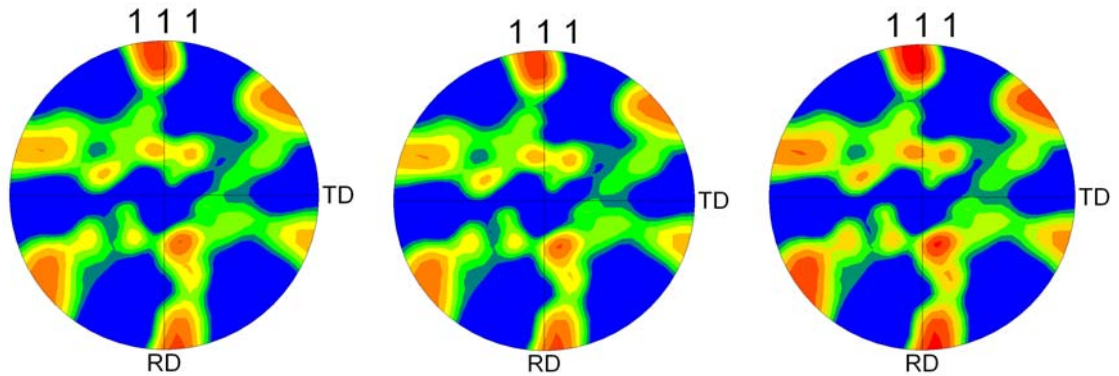


Figure 37: Pole Figures of Final Texture for Simple Shear with Thermal Softening for (left to right) a) 300/s, b) 1000/s, c) 3000/s.

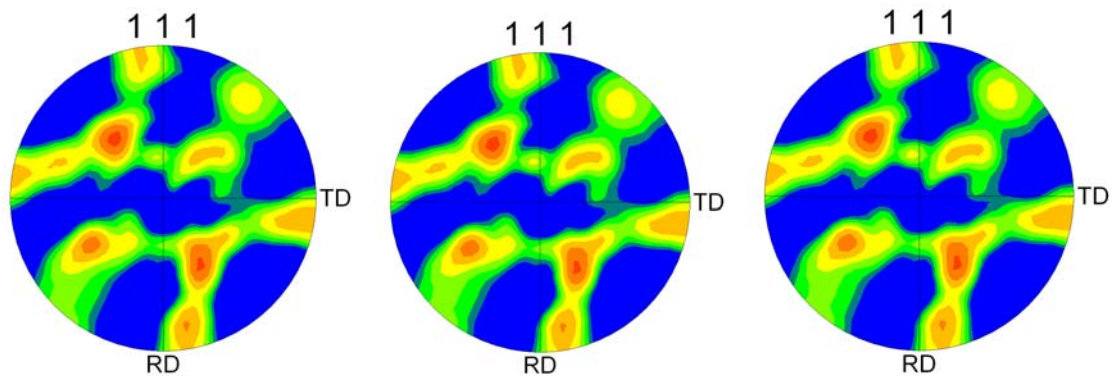


Figure 38: Pole Figures of Final Texture for Simultaneous Tension and Shear with Thermal Softening for (left to right) a) 300/s, b) 1000/s, c) 3000/s.

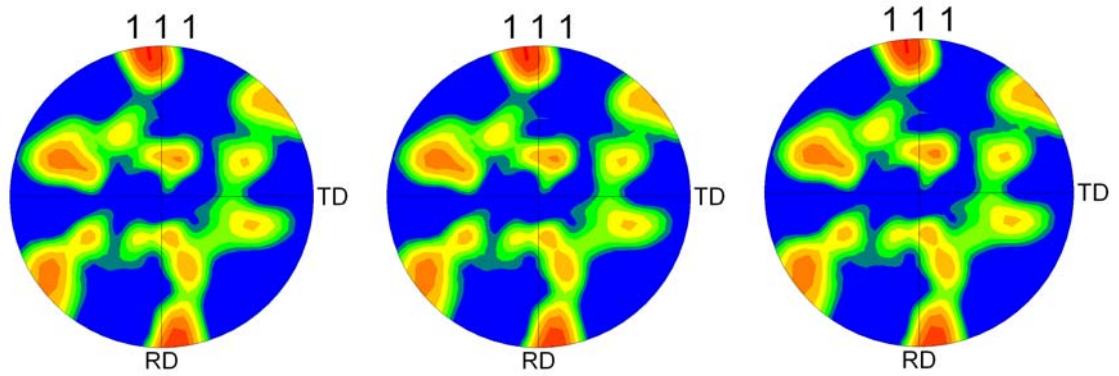


Figure 39: Pole Figures of Final Texture for Tension Followed by Shear with Thermal Softening for (left to right) a) 300/s, b) 1000/s, c) 3000/s.

Figure 40 shows disorientation of each element plotted on the undeformed grid. Figure 41 is a comparison between xy strain for the two strain paths also plotted on the undeformed grid for better comparison. As noted earlier, different strain paths show different shear bands developing. Both strain paths show that Cube, or near Cube, orientations have low values for disorientation angles while Goss orientations have high values for disorientation angles. This indicates that “Near Cube” orientations are stable orientations. The Cube oriented grains near the top right edge of the microstructure, marked as region 1 in the figure, show small rotations $\sim 10^\circ$ while the Goss grains marked as region 3 show large rotations up to a maximum of 32° . The amount of grain rotation seems to depend only on the original grain texture. The amount of local strain seems to have minimal effect on it.

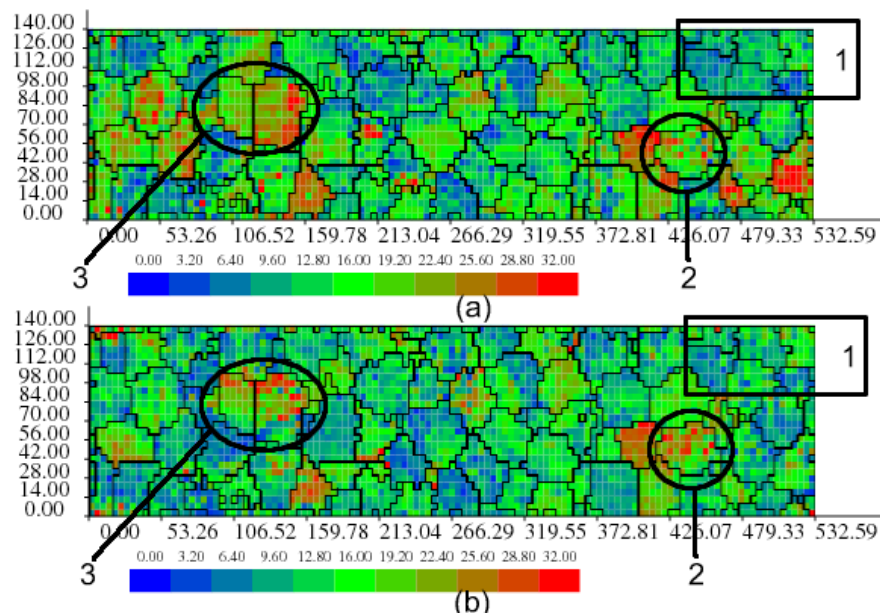


Figure 40: Showing the local lattice rotation for (a) simultaneous tension and shear and, (b) for tension followed by shear. Comparison shows cube orientation (ND rotated) is more stable than Goss.

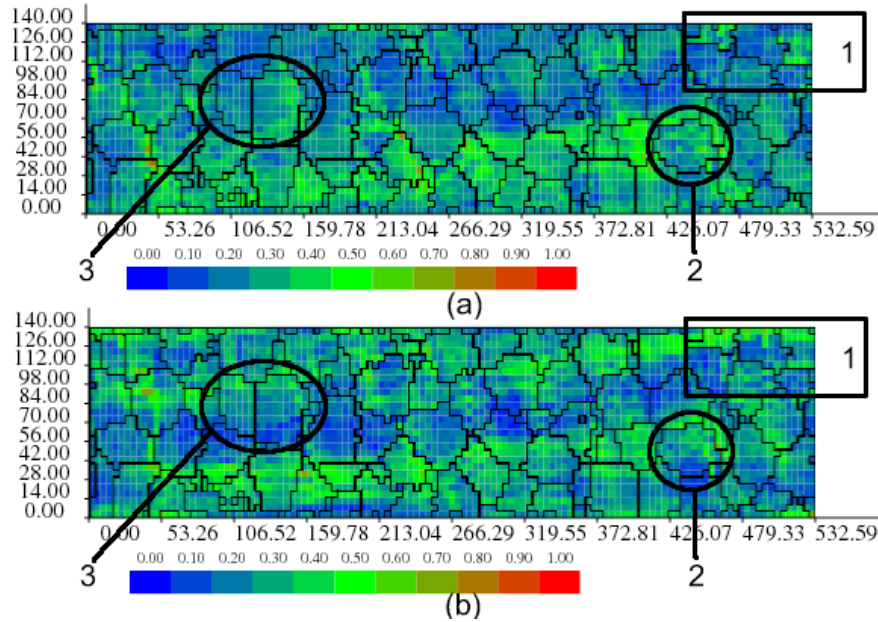


Figure 41: Showing the comparison between the xystrain for the two different strain paths. (a) Simultaneous tension and shear and (b) tension followed by shear

The cube grains in region 1 as well as the Goss grain in region 2 have a shear band passing through them for the case of tension followed by shear. While in the case of simultaneous tension and shear these regions have low local strain values as they are farther from the shear band. Irrespective of the local strain the cube grains show minimal rotation when the strain is low, as in the case of simultaneous tension and shear, or when it is high, as in the case for tension followed by shear. In contrast the Goss grains consistently show high rotations. The most notable exception is the cube grain located in region 2 which shows average amount of rotation $\sim 16^\circ$ for simultaneous tension and shear and has high rotation for the tension followed by shear case. In both cases it has significantly higher rotation than the cube grain in region 1.

Figure 42 shows the orientations of Cube-Near Cube grains in the center layers in regions 1 and 2 with 100 pole figure alongside. As noted earlier the grains in region 1 show minimal grain rotation while region 2 grain shows high rotation. The grains in region 1 show a rotated Cube orientation (ND rotated) as against the region 2 grain which shows exact Cube orientation. Figure 43 shows the orientation before and after deformation. The orientation of the grain after deformation shows ND rotated Cube orientation, which is a stable orientation.

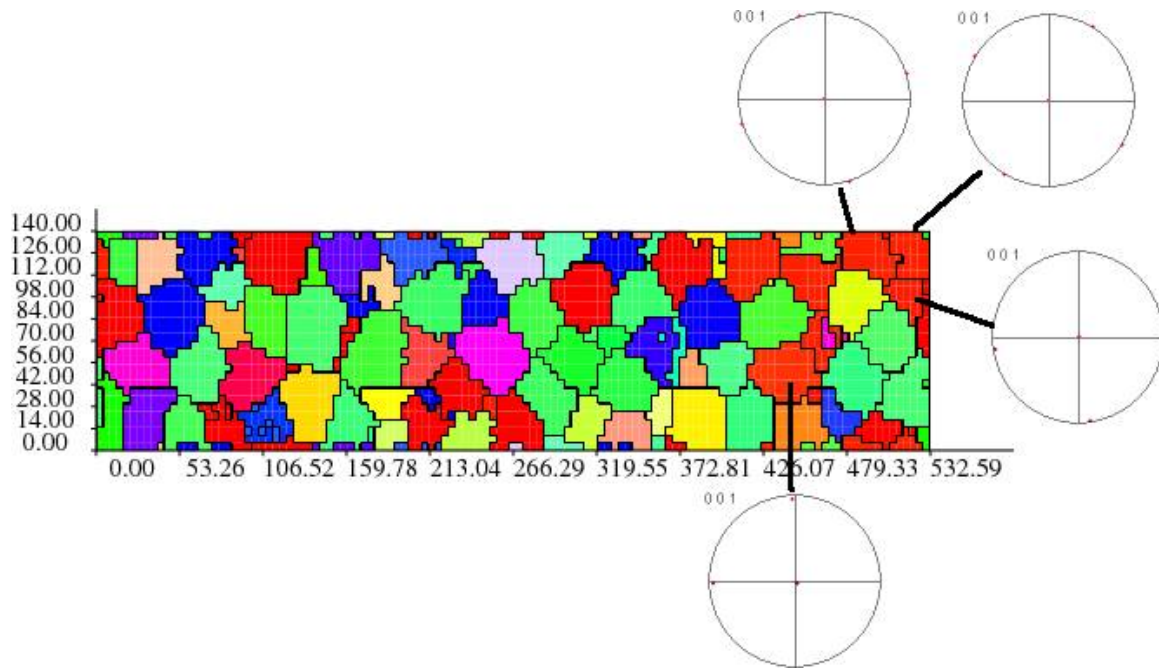


Figure 42: Showing the exact orientations of some of the near Cube grains

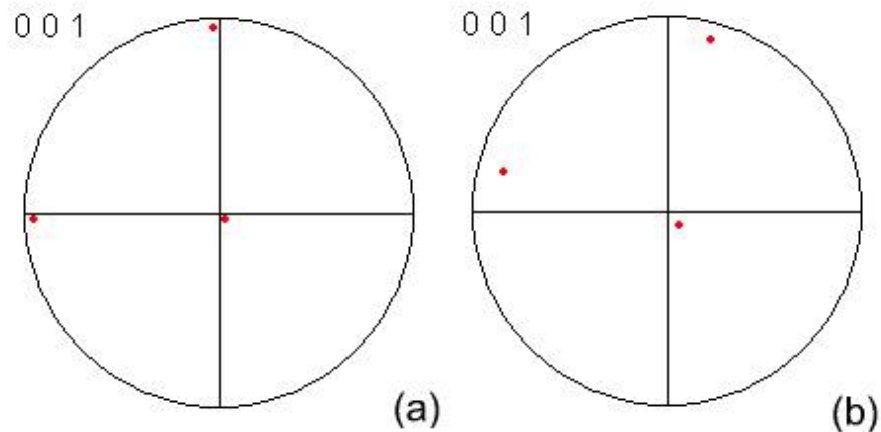


Figure 43: Orientation of grain in region 2 (a) before and (b) after deformation.

As can be seen in Table 5, the strain path with the highest average xy shear strain is when tension is followed by shear. Not only is the average shear strain highest, but this strain path has the highest standard deviation. This would indicate that the tension followed by shear strain path has more pronounced localization than the simultaneous tension and shear with the same final macroscopic deformation. To confirm this, Figure 21 shows more visible banding than Figure 22. This would indicate that, based on the assumptions made in this model, to improve formability of a material with a similar microstructure for a given process,

the process should be devised so that any areas subjected to both shear and tension are formed with simultaneous tension and shear as opposed to tension followed by shear.

These 3D simulations have allowed observations to be made on the distribution of strain and disorientation through the thickness of our sample. It was shown that the shear strain through the thickness of the sample does not vary greatly after large deformation. Therefore the strain at a given point is dependant on the orientations of all the grains in the through thickness at that point.

It should be noted that there is very little literature available on high strain rate shear experiments with which to compare these findings.

6. Conclusions

Significant decreases have been achieved in the run times since the new scheme avoids complex and time demanding mathematical operations such as the inversion of matrices and/or iterations. The new formulation can be considered very similar to the classical rate tangent formulation for the case $\theta = 0$ (equation 21). However, with the new formulation, any inversion operation (e.g. equation 24) is avoided. Note that inversions of relatively large matrices are very costly in terms of CPU time. Furthermore, the size of the matrix to be inverted in equation 24 depends directly on the total number of slip systems considered in the crystal plasticity analysis. Thus the larger the number of slip systems (e.g. BCC and HCP crystals) the larger the size of the matrix to be inverted and the more CPU time. However, the new proposed method does not have this direct dependency of total number of slip systems on the CPU time.

The proposed model was employed in two 3D simulations to investigate the effects of particles in FCC polycrystals, and the effects of strain path, strain rate, and thermal softening in Al5754. The particle and grain models were built using 3D grids of equal sized brick elements. Voxelized 3D grain data was used to assign orientations to all of the elements. The elements that lay within the volume of a particle were represented with a rigid material model while the remaining elements used the in house crystal plasticity model described. It should be noted that the following conclusions are based on the assumption that there is no grain boundary sliding, no de-cohesion between the matrix and the particle, and no fracturing of the particle.

The first application shows that particle locations are crucial in identifying the formation of a localized deformation. The texture initially favoured a band to form in the material. The results showed that when a particle was placed near the band, the strain increased in the band while a parallel band that intersected the particle contained nearly no strain. When a particle was placed directly in the band, the localization in the simulation was inhibited. The strain concentration caused by a particle is a function of the strain on the matrix if the particle were not there, which in and of itself is a function of the remaining particles. The peak strain in the material was located around a particle that was not moved in the last two simulations. The strain in that area increased significantly with the third simulation. The overall strain outside of the band increased to accommodate the lower strain around the moved particle.

Our simulations clearly indicate that to improve localized deformation predictions, it is critical to incorporate not only the accurate placement of particles in the microstructure but also the accurate spacing and distribution of particles with respect to each other.

Recently, Inal et al. (2002b) have concluded that neither the plane strain nor plane stress assumptions for modelling simple shear are capable of accurately predicting the initiation of localized deformation. The new model presented in this paper can incorporate the three dimensional aspects of grain morphologies and their interactions, and thus, can account for the full richness of heterogeneous deformation in the form of localized bands.

The results from the second application show that with the same texture, strain distribution was only dependant on the strain path. It should be noted that the second simulation was based on the assumption that there is no grain boundary sliding. The strain rate of the simulations did not alter the location of any bands nor did the addition of thermal softening. As the strain rate increased, the material acted more uniformly when thermal softening was excluded. The distribution of strain did not change, but the range in magnitudes decreased with the standard deviation while the average strain did not change. The average rotation decreased with higher strain rate. The texture also showed a stronger dependency with strain path than strain rate. Higher strain rates only succeeded in sharpening the pole figures. When thermal softening was included, the effect of strain rate increase could be correlated with a larger temperature rise. The decrease in average rotation when strain rate increased became more pronounced when thermal softening was included.

By comparing the simulated crystallographic rotation with and without thermal softening, for the strain paths considered, it appears as if geometrical softening dominates over thermal softening when strain rates are in the range of 300/s to 3000/s and dynamic recrystallization is excluded. Local geometrical differences such as grain orientation produced greater rotation heterogeneities than including or excluding thermal softening.

The concentrations in effective strain begin at grain boundaries in the simulations. When viewing the strain distribution at 1.5% macroscopic shear, the hot spots are focussed at the grain boundaries. The hot spots are different on each layer of the specimen at the beginning. As strain progresses, the strain distribution results become more uniform across the layers.

Initial orientation has the biggest impact on the amount of rotation seen within a grain regardless of the activity of the neighbouring grains. Strain distribution requires compatibility across through thicknesses causing grains to strain due to neighbouring grains when otherwise they would have not. Rotated Cube is a stable orientation and shows minimum grain reorientation while grains with initially Goss orientation show maximum grain rotation. Exact Cube orientation also rotates to a ND rotated Cube orientation. The Texture evolution is dominant and local rotation is independent of the local strain values as is evident from the

low rotation of the rotated Cube grains in region 1 and Goss grains in region 2 of Figure 40 and Figure 41.

Finally, the results from the second application show that texture evolution can not be accurately modelled by simple additive simulations; two completely different texture evolutions were predicted by two different strain paths even though both simulated the same effective macroscopic strain.

References

- Anand, L., Kalidindi, S.R., 1994, *The Process of Shear Band Formation in Plane Strain Compression of FCC Metals: Effects of Crystallographic Texture*. *Mechanics of Materials*, 17, 223-243.
- Anand, L., Kothari, M., 1996, *A computational procedure for rate independent crystal plasticity*. *Journal of the Mechanics and Physics of Solids*, 44, 524–558.
- Asaro, R. J., Needleman, A., 1985, *Texture development and strain hardening in rate dependent polycrystals*. *Acta Metallurgica*, 33, 923-953.
- Bardenhagen, S., Triantafyllidis, N., 1996, *The Influence of Scale size on the Stability of Periodic Solids and the Role of associated Higher Order Gradient Continuum Models*. *Journal of the Mechanics and Physics of Solids*, 44, 1891-1929.
- Beaudoin, A.J., Dawson, P.R., Mathur, K.K., Kocks, U.F, 1995, *A Hybrid Finite Element Formulation for Polycrystal Plasticity with Consideration of Macrostructural and Microstructural Linking*. *International Journal of Plasticity*, 11, 501-521.
- Beausir, B., Toth, L.S., Neale, K.W., 2007, *Role of strain-rate sensitivity in the crystal plasticity of hexagonal structures*. *International Journal of Plasticity* 23, 227-243.
- Belytschko, T., Liu, W. K., Moran, B., 2000, *Nonlinear Finite Elements for Continua and Structures*. John Wiley and Sons.
- Berveiller, M., Zaoui, A., 1978, *An Extension of the Self-Consistent Scheme to Plastically Flowing Crystals*. *Journal of the Mechanics and Physics of Solids*, 26, 325-344.
- Bishop, J.F.W., Hill, R., 1951a, *A theory of the Plastic Distortion of a Polycrystalline Aggregate under Combined Stresses*. *Philosophical Magazine*, 42, 414-427.
- Bishop, J.F.W., Hill, R., 1951b, *A Theoretical Derivation of the Plastic Properties of a Polycrystalline Face Centered Metal*. *Philosophical Magazine*, 42, 1298-1307.
- Bleck, W., Frehn, A., Larour, P., Steinbeck, G., 2004, *Investigations Concerning the Strain Rate Behaviour of Modern Sheet Steels for Autobody Applications*. *Materialwissenschaft und Werkstofftechnik*, 35(8), 505-513.
- Borg, U., 2007, *Strain gradient crystal plasticity effects on flow localization*. *International Journal of Plasticity* 23, 1400-1416.

- Borg, U., Niordson, C.F., Kysar, J.W., 2008, *Size effects on void growth in single crystals with distributed voids*. International Journal of Plasticity 24, 688-701.
- Brahme, A., Alvi, M., Saylor, D., Fridy, J., Rollett, A.D., 2007, *3D reconstruction of microstructure in a commercial purity aluminum*. Scripta Materialia, 55(1), 75-80.
- Brahme, A., Inal, K., Mishra, R.K., Saimoto, S., 2009, *The backstress effect of evolving deformation boundaries in FCC polycrystals*. (Submitted to Elsevier).
- Bridier, F., McDowell, D.L., Villechaise, P., Mendez, J., 2009, *Crystal plasticity modeling of slip activity in Ti-6Al-4V under high cycle fatigue loading*. International Journal of Plasticity 25, 1066-1082.
- Bronkhorst, C.A., Kalidindi, S.R., Anand, L., 1992, *Polycrystalline Plasticity and the Evolution of Crystallographic Texture in FCC Metals*. Philosophical Transactions of the Royal Society London, A341, 443-477.
- Budiansky, B., Wu, T.T., 1962, *Theoretical Prediction of Plastic Strains of Polycrystals*. Proceedings of the 4th Congress of Applied Mechanics, 1175.
- Canova, G.R., Kocks, U.F. and Jonas, J.J., 1984, *Theory of Torsion Texture Development*. Acta Metallurgica, 32, 211-226.
- Chin, G.Y., Mammel, W.L., 1969, *Generalisation and Equivalence of the Minimum Work (Taylor) and Maximum Work (Bishop-Hill) Principles for Crystal Plasticity*. Transactions of the Metallurgical Society AIME, 245, 1211-1214.
- Colvin, J.D., Minich, R.W., Kalantar, D.H., 2009, *A model for plasticity kinetics and its role in simulating the dynamic behaviour of Fe at high strain rates*. International Journal of Plasticity 25, 603-611.
- Cuitino, A. M., Ortiz, M., 1993, *Computational modeling of single-crystals*. Modelling and Simulation in Materials Science and Engineering, 1 (3), 225–263.
- Dawson, P., Boyce, D., MacEwen, S., Rogge, R., 1999, *Intercrystalline Stresses in Metal Polycrystals: Comparing Simulations To Diffraction Experiments*. ICOTOM 12, Montreal, NRC Research Press, 1, 505-510.
- Delannay, L., Jacques, P. J., Kalidindi, S. R., 2006, *Finite element modeling of crystal plasticity with grains shaped as truncated octahedrons*. International Journal of Plasticity 22, 1879-1898.

Delannay, L., Jacques, P. J., Pardeon, T., 2007, *Modelloing of the plastic flow of trip-aided multiphase steel based on an incremental mean-field approach*. International Journal of Solids and Structures 45, 1825-1843.

Delannay, L., Melchoir, M. A., Kanjarla, A. K., Van Houtte, P., and Signorelli, J. W., 2008, *CPFEM investigation of the effect of grain shape on the planar anisotropy and the shear banding of textured metal sheets*. Proceedings of the 15th International Conference on Textures of Materials (ICOTOM 15)

Drugan, W.J., Willis, J.R., 1996, *A Micromechanics-Based Nonlocal Constitutive Equation and Estimates of Representative Volume Element Size for Elastic Composites*. Journal of the Mechanics and Physics of Solids, 44, 497-524.

Eringen, A.C., 1968, *Theory of Micropolar Elasticity. Fracture, An Advanced Treatise*. H. Liebowitz, Editor, Academic Press, New York, 2, 621-729.

Eshelby, J.D., 1957, *The Deformation Behaviour of the Elastic Field of an Ellipsoidal Inclusion and Related Problems*. Proceedings of the Royal Society London., A241, 376-396.

Fleck, N.A., Hutchinson, J.W., 1993, *A Phenomenological Theory for Strain Gradient Effects in Plasticity*. Journal of the Mechanics and Physics of Solids, 41, 1825-1857.

Fleck, N.A., Hutchinson, J.W., 1997, *Strain Gradient Plasticity*. Advanced Applied Mechanics, 33, 296-361.

Fuh, S., Havner, K.S., 1989, *A Theory of Minimum Plastic Spin in Crystal Mechanics*. Proceedings of the Royal Society London., A422, 193-239.

Gan, Y.X., Kysar, J.W., 2007, *Cylindrical void in a rigid-ideally plastic single crystal III: Hexagonal close-packed crystal*. International Journal of Plasticity 23, 592-619.

Gan, Y.X., Kysar, J.W., Morse, T.L., 2006, *Cylindrical void in a rigid-ideally plastic single crystal II: Experiments and simulations*. International Journal of Plasticity 22, 39-72.

Gasparini, M., Richard, V., Chiron, R., 2001, *Development of Plastic Strain Heterogeneities on Cold-Rolled Aluminium Alloys During Insitu Shear Tests Inside a SEM*. Journal de Physique, 11, 221-228.

Graff, S., Brocks, W., Steglich, D., 2007, *Yielding of magnesium: From single crystal to polycrystalline aggregates*. International Journal of Plasticity 23, 1957-1978.

Hallquist, J. O., 1998, *LS-DYNA - Theoretical Manual*. Livermore Software Technology Corporation.

Harren, S.V., Deve, H.E., Asaro, R.J., 1988, *Shear Band Formation in Plane Strain Compression*. Acta Metallurgica, 36, 2435-2480.

Harren, S., Lowe, T.C., Asaro, R.J., Needleman, A., 1989, *Analysis of Large-Strain Shear in Rate-Dependent Face-Centered Cubic Polycrystals: Correlation of Micro- and Macromechanics*. Philosophical Transactions of the Royal Society London, A328, 443-500.

Hassan, T., Taleb, L., Krishna, S., 2008, *Influence of non-proportional loading on ratcheting responses and simulations by two recent cyclic plasticity models*. International Journal of Plasticity 24, 1863-1889.

Hill, R., 1965, *Continuum Micro-Mechanics of Elasto-Plastic Polycrystals*. Journal of Mechanics and Physics of Solids, 13, 89-101.

Holmedal, B., Van Houtte, P., An, Y., 2008, *A crystal plasticity model for strain-path changes in metals*. International Journal of Plasticity 24, 1360-1379.

Honneff, H., Mecking, H., 1978, *A Method for the Determination of the Active Slip Systems and Orientation Changes During Single Crystal Deformation*. Proceedings of ICOTOM 5, Aachen, Springer-Verlag, 1, 265-275.

Hosford, W. F., 1993, *The Mechanics of Crystals and Textured Polycrystals*. Oxford University Press.

Horstemeyer, M.F., McDowell, D.L., 1998, *Modelling effects of Dislocation Substructure in Polycrystal Elastoviscoplasticity*. Mechanics of Materials., 27, 145-163.

Hutchinson, J.W., Neale, K.W., 1978a, *Sheet Necking – II. Time-independent behaviour*. In: *Mechanics of Sheet Metal Forming*. D.P. Koistinen and N.M. Wang (Eds). Plenum Press, New York, pp. 127-153.

Hutchinson, J.W., Neale, K.W., 1978b, *Sheet Necking – III. Strain-rate effects*. In: *Mechanics of Sheet Metal Forming*. D.P. Koistinen and N.M. Wang (Eds). Plenum Press, New York, pp. 269-285.

Inal, K., Simha, H.M., Mishra, R., 2008, *Numerical Modeling of Second-Phase Particle Effects on Localized Deformation*. Journal of Engineering Materials and Technology, 130.

Inal, K., Wu, P. D., Neale, K. W., 2002a, *Finite element analysis of localization in FCC polycrystalline sheets under plane stress tension*. International Journal of Solids and Structures, 39, 3469–3486.

- Inal, K., Wu, P.D., Neale, K.W., 2002b, *Large Strain Behaviour of Aluminium Sheets Subjected to In-Plane Simple Shear*. Modelling and Simulation in Material Science and Engineering, 10, 237-252.
- Kakunai, S., Masaki, J., Kuroda, R., Iwata, K., Nagata, R., 1985, *Measurement of Apparent Young's Modulus in the Bending of Cantilever Beam by Heterodyne Holographic Interferometry*. Experimental Mechanics, 408-412.
- Kalidindi, S. R., Bronkhorst, C. A., Anand, L., 1992, *Crystallographic texture evolution in bulk deformation processing of fcc metals*. Journal of the Mechanics and Physics of Solids, 40 (3), 537–569.
- Kalidindi, S.R., Donohue, B.R., Li, S., 2009, *Modeling texture evolution in equal channel angular extrusion using crystal plasticity finite element models*. International Journal of Plasticity 25, 768-779.
- Kochendorfer, A., 1941, *Plastische Eigenschaften von Kristallen und Metallischen Werkstoffen*. Springer, Berlin.
- Kocks, U. F., 1970, *Relation Between Polycrystal Deformation and Single Crystal Deformation*. Metallurgical Transactions, 1 (5), 1121.
- Kocks, U.F., Canova, G.R., 1981, *How Many Slip Systems and Which?, Deformation of Polycrystals*. N. Hansen et al., Editors, Riso National Laboratory, Roskilde, Denmark, 35.
- Kocks, U. F., Tome, C. N., Wenk, H. R., Mecking, H., 2001, *Texture and Anisotropy*. Cambridge University Press.
- Koiter, W.T., 1964, *Couple Stresses in the Theory of Elasticity, I and II*. Proceedings of the Koninklijke Nederlands Akademie van Wetenschappen, B67, 17-44.
- Kröner, E., 1958, *Berechnung der Elastischen Konstanten des Vielkristalls aus den Konstanten des Einkristalls*. Zeitschrift für Physik, 151, 504-518.
- Kuchnicki, S. N., Cuitino, A. M., Radovitzky, R. A., 2006, *Efficient and robust constitutive integrators for single-crystal plasticity modeling*. International Journal of Plasticity, 22 (10), 1988–2011.
- Kuchnicki, S. N., Radovitzky, R. A., Cuitino, A. M., 2008, *An explicit formulation for multiscale modeling of bcc metals*. International Journal of Plasticity 24, 2173-2191.
- Kuhlmann-Wilsdorf, D., 1989, *Theory of Plastic Deformation: Properties of Low Energy Dislocation Structures*. Material Science and Engineering, A113, 1-41.

Leffers, T., 1992, *A Model for Rolling the Deformation with the Grains Subdivided into Cell Blocks*. Proceedings of the 13th Riso International Symposium on Material Science, 7.

Lemonds, J., Needleman, A., 1986, *Finite Element Analyses of Shear Localization in Rate and Temperature Dependent Solids*. Mechanics of Materials, 5, 339-361.

Lévesque, J., Inal, K., Neale, K.W., Mishra, R.K., 2009, *Numerical modeling of extruded magnesium alloy tubes*. International Journal of Plasticity, in press.

Li, H. W., Yang, H., Sun, Z. C., 2008, *A robust integration algorithm for implementing rate dependent crystal plasticity into explicit finite element method*. International Journal of Plasticity, 24, 267–288.

Ling, X. W., Horstemeyer, M. F., Potirniche, G. P., 2005, *On the numerical implementation of 3d rate-dependent single crystal plasticity formulations*. International Journal for Numerical Methods in Engineering, 63 (4), 548–568.

Ma, Q., Clarke, D.R., 1995, *Size Dependent Hardness of Single Crystals*. Journal of Materials Research, 10, 853-863.

Maniatty, A. M., Dawson, P. R., Lee, Y. S., 1992, *A time integration algorithm for elastoviscoplastic cubic-crystals applied to modeling polycrystalline deformation*. International Journal for Numerical Methods in Engineering, 35 (8), 1565–1588.

Mathur, K.K., Dawson, P., 1989, *On modelling the Development of Crystallographic Texture in Bulk Forming Processes*. International Journal of Plasticity, 5, 69-94.

Mathur, K.K., Dawson, P., Kocks, U.F., 1990, *On Modelling Anisotropy in Deformation Processes Involving Textured Polycrystals with Distorted Grain Shape*. Mechanics of Materials, 10, 183-202.

Mayeur, J.R., McDowell, D.L., 2007, *A three-dimensional crystal plasticity model for duplex Ti-6Al-4V*. International Journal of Plasticity 23, 1457-1485.

Mckinley, J., Simha, H., Worswick, M., 2009, *Constitutive Modelling of Aluminum Clad Sheet for Warm Forming*. Internation Deep Drawing Research Group.

Mindlin, R.D., 1963, *Influence of Couple-Stresses on Stress Concentrations*. Experimental Mechanics, 3, 1-7.

Mindlin, R.D., 1964, *Micro-Structure in Linear Elasticity*. Archive for Mechanics and Analysis, 16, 51-78.

Mindlin, R.D., 1965, *Second Gradient of Strain and Surface Tension in Linear Elasticity*. International Journal of Solids and Structures, 1, 417-438.

- Mughrabi, H., 1983, *Dislocation Wall and Cell Structures and Long Range Internal Stresses in Deformed Metal Crystals*. Acta Metallurgica Materialia, 31, 1367-1379.
- Peirce, D., Asaro, R. J., Needleman, A., 1982, *An Analysis of Nonuniform and Localized Deformation in Ductile Single Crystals*. Acta Metallurgica, 30, 1087–1119.
- Peirce, D., Asaro, R. J., Needleman, A., 1983, *Material rate dependence and localized deformation in crystalline solids*. Acta Metallurgica, 31 (12), 1951–1976.
- Peirce, D., Shih, C. F., Needleman, A., 1984, *A tangent modulus method for rate dependent solids*. Computers and Structures, 18 (5), 875–887.
- Qu, S., Siegmund, T., Huang, Y., Wu, P.D., Zhang, F., Hwang, K.C., 2005, *A study of particle size effect and interface fracture in aluminum alloy composite via an extended conventional theory of mechanism-based strain-gradient plasticity*. Composites Science and Technology, 65, 1244-1253.
- Radhakrishnan, B., Sarma, G., Weiland, H., Baggethun, P., 2000, *Simulations of deformation and recrystallization of single crystals of aluminium containing hard particles*. Modelling and Simulation in Materials Science and Engineering, 8, 737-750.
- Raphanel, J. L., Ravichandran, G., Leroy, Y. M., 2004, *Three-dimensional rate-dependent crystal plasticity based on Runge-Kutta algorithms for update and consistent linearization*. International Journal of Solids and Structures, 41 (22-23), 5995–6021.
- Rashid, M.M., Nemat-Nasser, S., 1990, *A Constitutive Algorithm for Rate Dependent Crystal Plasticity*. Computer Methods in Applied Mechanics and Engineering, 94, 201-228.
- Rauch, E.F., 1997, *Plastic Anisotropy of Sheet Metals Determined by Simple Shear Tests*. Materials Science and Engineering, A241, 179-183.
- Renouard, M., Wintenberger, M., 1976, *Homogeneous Deformation of EFC crystals by Glide of Dislocations with Imposed Stresses and Strains*. Comptes Rendous Hebdomadaires Des Seances De L'Academie Des Sciences Serie B, 283 (8), 237-240
- Rossiter, J., Brahme, A., Inal, K., Mishra, R.K., 2009a, *A new Crystal Plasticity Scheme for Explicit Time Integration Codes to Simulate Deformation in 3D Microstructures: Part 2: Effects of Strain path, Strain Rate and Thermal Softening on Localized Deformation in the Aluminum Alloy 5754 During Simple Shear*. (submitted to IJP)
- Rossiter, J., Brahme, A., Simha, H., Inal, K., Mishra, R.K., 2009b, *A new Crystal Plasticity Scheme for Explicit Time Integration Codes to Simulate Deformation in 3D Microstructures: Part 1: Non-homogeneous deformation in multiphase microstructures*. (submitted to IJP)

Sachs, G., 1928, *Zur Ableitung einer Fließbedingung*. Zeitschrift des Vereines Deutscher Ingenieure, 72, 734-736.

Sarma, G.B., Dawson, P., 1996a, *Effects of Interactions Among Crystals on the Inhomogeneous deformation of Polycrystals*. Acta Materialia, 44, 1937-1953.

Sarma, G.B., Dawson, P., 1996b, *Texture Predictions Using A Polycrystal Plasticity Model Incorporating Neighbor Interactions*. International Journal of Plasticity, 12, 1023-1054.

Schaffer, M., Wagner, J., Schaffer, B., Schmied, B., Mulders, H., 2007, *Automated three-dimensional X-ray analysis using a dual-beam FIB*. Ultramicroscopy, 107, 587-597.

Schmid, E., 1924, *Neuere Untersuchungen Metallkristallen*. Proceedings of the 1st International Congress for Applied Mechanics, C.B Biezeno and J.M. Burgers, Editors, Delft, The Netherlands, 342-353.

Shan, Z. and Gokhale, A.M., 2002, *Representative volume element for non-uniform microstructure*. Computational Materials Science 24, pp. 361-379.

Shen, H., and Lissenden, C.J., 2002, *3D finite element analysis of particle-reinforced aluminum*. Materials Science and Engineering A338, 271-281.

Simha, M.H., Inal, K., and Worswick, J.M., 2008, *Path and Orientation Dependence of Formability in the Stress- and Extended Stress-Based Forming limit Curves*. The Journal of Engineering Materials and Technology, 130, 2003 – 2011.

Spowart, J., Mullens, H., Puchala, B., 2003, *Collecting and analyzing microstructures in three dimensions: A fully automated approach*. JOM, 55, 35-37.

Stelmashenko, N.A., Walls, M.G., Brown, L.M., Milman, Y.V., 1993, *Microindentations on W and Mo Oriented Single Crystals: An STM Study*. Acta Metallurgica Materialia, 41, 2855-2865.

Taylor, G.I., 1934, *The Mechanism of Plastic Deformation of Crystals*. Proceedings of the Royal Society London, A165, 253-257.

Taylor, G.I., 1938, *Plastic Strain in Metals*. Journal Institute of Metals, 62, 307-324.

Taylor, G.I., Elam, C.F., 1923, *The Distortion of an Aluminium Crystal During a Tensile Test*. Proceedings of the Royal Society London, A102, 643-661.

Tang, C.Y., Lee, T.C., Rao, B., 2003, *An Experimental Study of Shear Damage and Failure of Aluminium Alloy 2024T3*. Journal of Materials Processing Technology, 139,208-211.

Tewari, A., Tiwari, S.M., Biswas, P., Vijayalakshmi, S., Mishra, R.K., 2009, *Vectorized 3D Microstructure for Finite Element Simulations*. Submitted to Materials Characterization.

Tome, C., Canova, G.R., Kocks, U.F., Christodoulou, N., JONAS, J.J., 1984, *The Relation Between Macroscopic and Microscopic Strain Hardening in FCC Polycrystals*. Acta Metallurgica, 32, 1637-1653.

Toupin, R.A., 1962, *Elastic Materials with Couple Stresses*. Archive for Rational Mechanics and Analysis, 11, 385-414.

Van Den Boogaard, A.H., Huetink, J., 2006, *Simulation of Aluminium Sheet Forming at Elevated Temperatures*. Computer Methods in Applied Mechanics and Engineering, 195, 6691-6709.

Van Der Giessen, E., Needleman, A., 1995, *Discrete Dislocation Plasticity: A Simple Planar Model*. Modelling and Simulation in Materials Science and Engineering, 3, 689-735.

Voyiadjis, G.Z., Huang, W., 1996, *A modelling of Single Crystal Plasticity with Backstress Evolution*. European Journal of Mechanics, A/Solids, 15, 553-573.

Zaefferer, S., Wright, S.I., Raabe, D., 2008, *Three-dimensional orientation microscopy in a focused ion beam-scanning electron microscope: A new dimension of microstructure characterization*. Metallurgical and Materials Transactions A 39A, 374-389.

Zamiri, A., Pourboghra, F., Barlat, F., 2007, *An effective computational algorithm for rate-independent crystal plasticity based on a single crystal yield surface with an application to tube hydroforming*. International Journal of Plasticity, 23, 1126-1147.

Zhang, F., Bower, A.F., Mishra, R.K., Boyle, K.P., 2009, *Numerical simulations of necking during tensile deformation of aluminum single crystals*. International Journal of Plasticity 25, 49-69.

Zhang, M., Zhang, J., McDowell, D.L., 2007, *Microstructure-based crystal plasticity modeling of cyclic deformation of Ti-6Al-4V*. International Journal of Plasticity 23, 1328-1348.

Zikry, M. A., 1994, *An accurate and stable algorithm for high strain-rate finite strain plasticity*. Computers and Structures, 50 (3), 337-350.

Zikry, M. A., Nemat-Nasser, S., 1990, *High Strain-Rate Localization and Failure of Crystalline Materials*. Mechanics of Materials, 10 (3), 215-237.

Zuiker, J., Dvorak, G., 1994, *The Effective Properties of Functionally Graded Composites-I. Extension of the Mori-Tanaka method to Linearly Varying Fields*. Composites Engineering, 4, 19-35.